Interaction between water-saturated Kosa particles and polycyclic aromatic hydrocarbons

Lulu Zhang

July 2020

博 士 論 文

Interaction between water-saturated Kosa particles and polycyclic aromatic hydrocarbons

飽湿状態における黄砂と多環芳香族炭化水素との相互作用に関する研究

<div align="right">

金沢大学大学院医薬保健学総合研究科

創薬科学専攻

環日連携研究グループ

</div>

学 籍 番 号：1729012006

氏 名：張 露露

主任指導教員名：唐 寧

Abstract

Kosa (Asian dust) is a large contributor to atmospheric aerosols and has attracted worldwide attention for posing a large challenge to global climate, visibility, and human health. East Asia is one of the world's largest dust sources. Moreover, East Asian countries, especially China, are macroconsumers of fossil and biomass fuels, where both parent and substituted polycyclic aromatic hydrocarbons (PAHs) remain at high levels in the atmosphere. During the prevalence of Kosa, a simultaneous increase in Kosa particles and particulate PAHs has been sometimes observed in downwind areas, and a rapid production of PAH derivatives has been observed in the later Kosa episode. Therefore, Kosa particles are believed to act as carriers for PAHs during long-range transportation. The heterogeneous interaction between Kosa and PAHs may lead to worsened air quality and enhanced cytotoxicity and carcinogenicity of ambient particulates in downwind areas. The purpose of this study was to clarify the primitive function of Kosa on PAHs, which may drive the atmospheric behavior of PAHs, the generation of secondary aerosols and their health effects. Naphthalene (Nap) was chosen as the model PAH because of its high water solubility and vapor pressure, simple structure, and atmospheric abundance. In this study, the heterogeneous interactions between Nap and different Kosa particles were investigated in aqueous systems, considering the complex mineralogy and hygroscopicity of Kosa. The main results of this study are shown as follows:

(1) The Kosa samples used in this study were collected from typical Asian deserts, including the Gobi Desert, Taklimakan Desert, Horqin Sandy Land and Loess Plateau. The particle size, specific surface area, and porosity of the Kosa samples were measured. Moreover, fifteen metallic elements and nine water-soluble inorganic ions of each Kosa sample were detected. Both the physical and chemical properties of the Kosa samples varied with geographic origin. The Kosa sample from the Loess Plateau had the finest particle size

1

and the largest specific surface area and total pore volume, while the particle and pore size were uniform among the other three Kosa samples. The four Kosa samples were characterized by a high content of crustal elements and a low level of transition metals, whereas the mass fraction of each element varied largely. In addition, these four Kosa samples had different compositions on water-soluble inorganic ions, but the main components all were deliquescent salts.

(2) Batch adsorption experiments were performed to evaluate the adsorption capacity of each Kosa sample to Nap. The results showed that Kosa particles from the Loess Plateau had weak adsorption to Nap, which was fitted by the Langmuir isotherm. There was no obvious adsorption to Nap found for the other three Kosa samples. This difference seemed to depend mainly on the specific surface area and/or the total pore volume. However, the adsorption capacity of zeolites, a microporous mineral, was substantially higher than that of the Kosa samples investigated. In addition, acid conditions inhibited the adsorption of Kosa particles to Nap. Thus, Kosa particles exhibit a weak or negligible adsorption effect on Nap and have little superiority in adsorbing more hydrophobic PAHs.

(3) The reactivity experiments were performed under various conditions. The Nap in the aqueous solution did not undergo chemical reactions under dark conditions and longwave UV radiation but degraded under shortwave UV radiation, and 2-formylcinnamaldehyde and 1,4-naphthoquinone were the first-generated products. The degradation of Nap in the aqueous solution was probably initiated by photoionization, and the reaction rate constant (between 1.44×10^{-4} min^{-1} and 8.55×10^{-4} min^{-1}) was much lower than that of Nap with hydroxyl radicals. Interestingly, instead of inducing or promoting the chemical change in Nap, the Kosa particles slowed photodegradation due to the extinction of radiation. In addition, acid conditions may not significantly promote the photodegradation of Nap in the saturated water layer of the Kosa particles. Therefore, the Kosa particles played a less

2

important role in promoting the photodegradation of Nap than UV intensity and water content, which was independent of the difference in Kosa properties.

In conclusion, this laboratory study revealed that Kosa particles had little promotion on the adsorption and photodegradation of Nap, which suggests that Kosa originated from the Asian continent has no substantial interaction with PAHs in the atmosphere.

Abbreviations

Al	Aluminum
Al_2O_3	Aluminum oxide
Ba	Barium
BET	Brunauer-Emmett-Teller
$Ca(NO_3)_2$	Calcium nitrate
Ca^{2+}	Calcium ion
$CaCO_3$	Calcium carbonate
CaO	Calcium oxide
Cl^-	Chloride ion
Cu	Copper
F^-	Fluoride ion
2-FCA	2-Formylcinnamaldehyde
Fe	Iron
Fe_2O_3	Iron oxide
GC-MS	Gas chromatography-mass spectrometry
H_2O_2	Hydrogen peroxide
H_2SO_4	Sulfuric acid
HCl	Hydrochloric acid
HF	Hydrofluoric acid
HNO_3	Nitric acid
HPLC	High-performance liquid chromatography
IC	Ion chromatography
K	Potassium
K^+	Potassium ion
KUWAMS	Kanazawa University Wajima Air Mornitoring Station
m/z	Mass-to-charge ratio
Mg^{2+}	Magnesium ion
MgO	Magnesium oxide
Mn	Manganese

|	
Na^+	Sodium ion
Na_2CO_3	Sodium carbonate
Na_2SO_4	Sodium sulfate
NaCl	Sodium chloride
$NaHCO_3$	Sodium bicarbonate
Nap	Naphthalene
1, 4-NQ	1, 4-Naphthoquinone
NH_3	Ammonia
NH_4^+	Ammonium ion
Ni	Nickel
NO_2	Nitrogen dioxide
NO_3	Nitro radical
NO_3^-	Nitrate ion
O_2	Oxygen
O_3	Ozone
OH	Hydroxyl group/radical
P	Phosphorus
PAHs	Polycyclic aromatic hydrocarbons
PTFE	Polytetrafluoroethylene
ROS	Reactive oxygen species
RSD	Relative standard deviation
Sc	Scandium
Si	Silicon
SiO_2	Silica
SO_2	Sulfur dioxide
SO_4^{2-}	Sulfate ion
SOA	Secondary organic aerosols
Sr	Strontium
Ti	Titanium
UV	Ultraviolet
Zn	Zinc

Contents

Background

Polycyclic aromatic hydrocarbons (PAHs) are a kind of environmental hormones that are ubiquitous in the atmosphere (Brody et al., 2007; Ying et al., 2017). Numerous studies have demonstrated the carcinogenic and mutagenic potential of PAHs (Bollinger et al., 2015; Nisbet and Lagoy, 1992; Pavanello and Lotti, 2013), and the induction of oxidative stress and DNA damage (Jeng et al., 2011; Quintana et al., 2008; Tang et al., 2006), which increases the health risks in humans (Liu et al., 2016; Zhang et al., 2019, 2020a). Incomplete combustion of organic materials, such as oil, coal, and biomass, is a considerable source of PAHs (Khalili et al., 1995; Mitra et al., 1987). After being released into the atmosphere, PAHs undergo dynamic transitions between the particle and gas phases in response to the changes in vapor pressure. Mostly, PAHs with low molecular weight prone to be distributed in the gas phase, while those with high molecular weight have a preference to bind particulate matter (Araki et al., 2009). Furthermore, PAHs can be converted to various derivatives through gas phase or multiphase reactions (Arey et al., 1986; Bedjanian et al., 2010). Among the derivatives, oxygenated and nitrated PAHs have direct-acting mutagenicity and can increase the generation of reactive oxygen species (ROS) (Ames et al., 1975; Durant et al., 1996; Hayakawa, 2016; Jariyasopit et al., 2014). On the other hand, PAH derivatives have higher chemical activity than the parent PAHs and are nonnegligible precursors of secondary organic aerosols (SOA) (El zein et al., 2019). Therefore, PAHs and their derivatives pose a threat to the atmospheric environment and human health.

Globally, China is the country with the highest annual energy consumption, which accounted for 50.7% and 14.2% of the global consumption of coal and oil in 2018, respectively (BP p.l.c., 2019). As a result, atmospheric PAHs in China are at a relatively high level and can enhance the PAH pollutions in downwind countries or regions through short-

or long-range transport (Shimada et al., 2020; Sofowote et al., 2011; Tang et al., 2017; Wei et al., 2019). In particular, coal heating in Northern China is routine from November to April of the following year, which increases local pollution emissions and the pollutants transported southeastward via the East Asian winter monsoon (Lang et al., 2008). This exogenous influence was keenly reflected by the long-term variations in PAHs observed at Kanazawa University Wajima Air Monitoring Station (KUWAMS), a background site in Western Japan, and was confirmed by trajectory model estimations (Tang et al., 2005; Yang et al., 2007, 2009; Tang et al., 2014, 2015; Zhang et al., 2020b). **Fig. 1** shows the monthly concentration of particulate PAHs at KUWAMS from October 2004 to April 2020, which was remarkably higher during the heating period in Northern China than that in other months (Tang et al., 2015; Zhang et al., 2020b). Interestingly, during some Kosa events, the concentration of PAHs at KUWAMS rose sharply (Yang et al., 2007, 2009). The simultaneous enhancement in Kosa and PAH pollution has also been observed in other downwind areas (Fang et al., 2005; Tamamura et al., 2007). Moreover, there was a dramatic increase in PAH derivatives in the later Kosa period in Beijing (Kameda et al., 2016). Based on the mineralogy of Kosa, such as metallic elements and oxides, the surface of Kosa particles has catalytic activity and the ability to adsorb trace gases (He et al., 2015; Ma et al., 2010). Therefore, Kosa was preconceived as an important carrier of PAHs (Inomata et al., 2017; Jia et al., 2015; Ren et al., 2019).
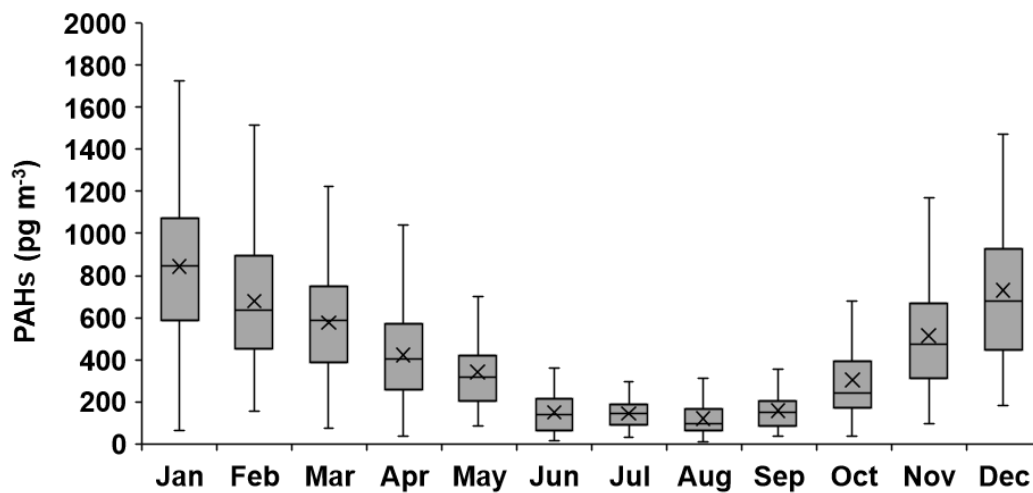
Fig. 1. Box plot of monthly concentration of particulate PAHs at Kanazawa University Wajima Air Monitoring Station (KUWAMS) from October 2004 to April 2020 (Tang et al., 2015; Zhang et al., 2020b). The upper and lower horizontal lines of the box are the third and first quartiles, respectively. The horizontal line in the middle of the box is the median. The cross in the box is the mean value. The upper and lower whiskers are the maximum and minimum, respectively.

Arid and semi-arid regions in Asia are mainly distributed in China, Mongolia, and some Central Asian countries, where Kosa is active in winter and spring (Kurosaki and Mikami, 2003; Shao and Dong, 2006). According to the 30-y records of the Japan Meteorological Agency (**Fig. 2**), Kosa was prevalent in Japan from February to May and mostly in March and April (JMA, 2020). This period overlapped with the heating period in Northern China that created opportunities for the encounter and interaction between Kosa and PAHs. However, there were some observations indicating that the Kosa events were insignificantly related to the PAH levels in downwind areas (Chio et al., 2012; Guo et al., 2003; Kim et al, 2012). The relationship between Kosa and PAHs might be influenced by the properties and transport pathway of Kosa and the aging of the air mass (Tamanura et al., 2007; Tang et al., 2014). The inconsistency of these observations makes the interaction between Kosa and PAHs more perplexing.
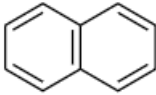
Some studies have shown that the heterogeneous interaction between mineral particles and gaseous molecules follows the Langmuir-Hinshelwood mechanism (Baxter and Hu, 2002; He et al., 2015). Briefly, two gaseous molecules adsorb on the particle surface and then react as they diffuse on the surface. The Langmuir-Hinshelwood mechanism has also been used to explain the increase of PAHs and their derivatives in atmospheric particulates during the Kosa periods (Kameda et al., 2016; Shimada et al., 2020; Shiraiwa et al., 2009). However, the adsorption and reactivity of Kosa particle to PAHs have not yet been studied in depth. On the other hand, the interaction between Kosa and PAHs will cause a double burden on air pollution and human health in downwind areas (Zhang et al., 2020c). Furthermore, the co-deposition of Kosa and PAHs will increase the pollution load of water and soil and cause the accumulation of PAHs in the organism and food chain (Hellou and Leonard, 2004; Logan, 2007). Therefore, it is urgent to figure out the substantial effect of Kosa particles on the transportation and conversion of PAHs in the atmosphere.
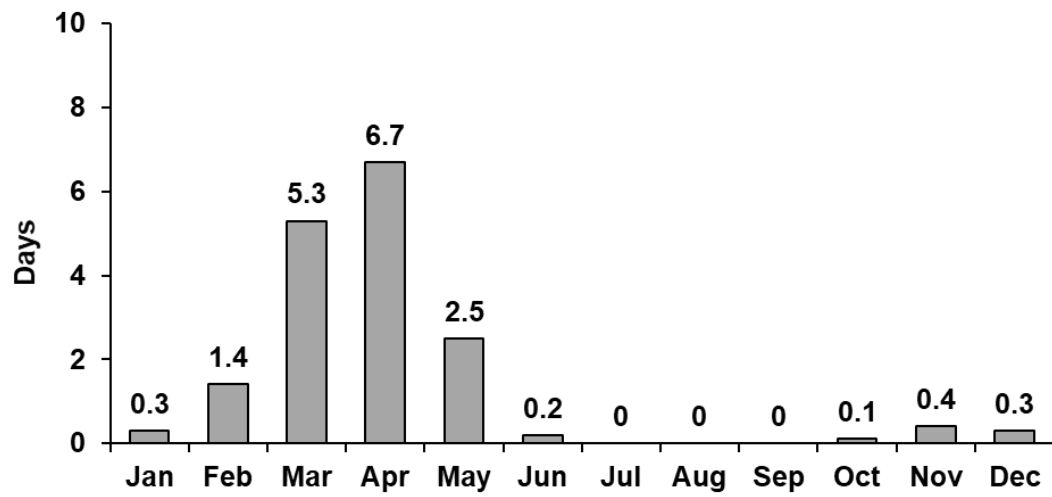
Fig. 2. Average monthly number of days with Kosa observed at eleven stations of the Japan Meteorological Agency from 1981 to 2010 (JMA, 2020).

The purpose of this study was to clarify the physical and chemical interaction between Kosa particles and PAHs. In this study, naphthalene (Nap) was used as the probe PAH due to the simple structure, and the high water-solubility and atmospheric abundance (Mastral and Callén, 2000). The properties of Nap are shown in **Table 1**. The authentic Kosa samples were collected from typical deserts in East Asia, and their physical characteristics and chemical compositions were measured. The adsorption capacity of different Kosa samples to Nap was then evaluated by batch adsorption experiments. In addition, batch reactivity experiments were performed under different conditions in an aqueous system to simulate the hygroscopicity of Kosa particles and investigate the reactivity of Nap on the water-saturated Kosa particles. The results of this study provide illuminating insights into the interaction between Kosa particles and PAHs, which contribute to bridge the gap between preconceptions and the essential role of Kosa and improve the comprehensive understanding of atmospheric processes.

Table 1. Properties of Naphthalene (Nap) (NCBI, PubChem Database).

Property	
Structure	
Molecular weight	128.17 g/mol (at 25°C)
Vapor pressure	11 Pa (at 25°C)
Water solubility	31 mg/L (at 25°C)
Toxicity	Causing acute and delayed toxicity and hemolysis [a]
	A possible carcinogen [b]

[a] Robles, 2014. [b] IARC, 2013.

Chapter 1. Physical properties and chemical compositions of different Kosa particles

1 Introduction

Deserts in China are mainly distributed in the north inland, covering a total area of more than 3.5 million km^2 (Shao and Dong, 2006). Each desert developed its own characteristics as the result of its origin and evolution. For example, the formation of the Gobi Desert and Taklimakan Desert, the most famous deserts in China, was mainly driven by climate factors (IGSNRR, CAS, 2007). The China Loess Plateau was formed by the displacement and deposition of dust from some deserts in Central Asia, and the loess that characterized by silty sand was then produced by geomorphic influences and rock weathering (Sun, 2002). Rather than natural formation, the Horqin Sandy Land, the largest sand land in China, originated from desertification caused by human activities (Bagan et al., 2010).

The physical properties of Kosa particles mainly include size, surface, and pore characteristics. The porosity (characterized by pore size and total pore volume) and pore structure of Kosa particles are dominated by diagenesis and desert soil development (He et al., 2019; Islam, 2009); whereas the shape and size of the original rock depend on the breakdown and abrasion caused by physical weathering and the joint effects of chemical and biological weathering (Carroll, 2012; Oliva et al., 2003). The specific surface area and porosity of particles are considered as key factors of adsorption performance, which affect the adsorption capacity and selectivity to adsorbates (Smol and Włodarczyk-Makuła, 2017; Yakout et al., 2013).

Kosa particles consist of a variety of minerals, which is influenced by the sedimentary environment and mineral maturity (Xu et al., 2008). Generally, the main minerals of Asian

desert soil are feldspar (aluminosilicates of calcium, sodium, potassium, and barium), quartz (silica), carbonatites, and metallic oxides (Jeong, 2008; Tang et al., 2019). The mineralogic composition of Kosa particles produces an effect on their atmospheric behavior (Cwiertny et al., 2008). For example, metallic oxides, such as silica (SiO_2), aluminium oxide (Al_2O_3), magnesium oxide (MgO), and calcium oxide (CaO), can alter the surface acidity of Kosa particles, leading to different adsorption of gas molecules, such as basic gas ammonia (NH_3) and acidic gases nitrogen dioxide (NO_2) and sulfur dioxide (SO_2) (He et al., 2015; Yang et al., 2018). Moreover, Kosa particles rich in Al and Ca have higher adsorption efficiency for polar volatile organic compounds (Zeineddine et al., 2018). In addition, iron oxide (Fe_2O_3) can affect the redox properties of the particle surface (Yang et al., 2018), whereas the ions and oxides of copper (Cu), manganese (Mn), and titanium (Ti) can act as catalysts for surface reactions (Xu et al., 2019; Zhao et al., 2019; Zhu and Zhou, 2019).

Recently, the hygroscopicity of Kosa particles has attracted much attention because of the importance in atmospheric aqueous reactions and cloud condensation nuclei activities (Chen et al., 2020; Ma et al., 2012; Yamashita et al., 2011). The hygroscopicity of Kosa particles is associated with the composition of water-soluble inorganic ions. The main components of deliquescent salts include ions of sodium (Na^+), Ca^{2+}, Mg^{2+}, chloride (Cl^-), sulfate (SO_4^{2-}), and nitrate (NO_3^-), which have a positive effect on the hygroscopicity of Kosa particles (Osada, 2013; Tang et al., 2019). Moreover, Kosa particles rich in Al and Fe can effectively attract water from the atmosphere at low humidity levels (Zeineddine et al., 2018). The water layer formed on the surface of Kosa particles can change the phase and reaction path of gaseous compounds and improve the formation of secondary aerosols, thus it is an important interface for the heterogeneous chemistry of the troposphere (Tang et al., 2016).

From the above, the atmospheric behavior of Kosa particles mainly depends on their physical and chemical properties. To better understand the physical and chemical effects of

Kosa particles on PAHs, Kosa samples were collected from the Gobi Desert, Taklimakan Desert, Horqin Sandy Land, and Loess Plateau, and their physical properties and chemical compositions were measured.

2 Materials and methods

2.1 Materials

Two reference Kosa samples CJ 1 and CJ 2 were obtained from the National Institute for Environmental Studies (Certified Reference Material, Tokyo, Japan). Four internal standards XSTC-331, XSTC-1, XSTC-7, and XSTC-8 for elemental analysis were purchased from SPEX CertiPrep (NJ, US). Hydrogen peroxide (H_2O_2), hydrofluoric acid (HF), nitric acid (HNO_3), 2,6-pyridinedicarboxylic acid, sodium carbonate (Na_2CO_3) and sodium bicarbonate ($NaHCO_3$) were provided by Wako Pure Chemical Industries, Ltd. (Osaka, Japan). Ultrapure water (18.2 MΩ cm, 25°C) was prepared by a water purifier (H2OPRO-UV-T, Sartorius Lab Instruments GmbH εt Co. KG, Göttingen, Germany). All chemicals used in this study were of analytical reagent grade.

2.2 Collection of Kosa particles

The Kosa samples were collected from typical deserts in East Asia, including the Gobi Desert (Kosa 1), Taklimakan Desert (Kosa 2), Horqin Sandy Land (Kosa 3), and Loess Plateau (Kosa 4). **Fig. 1-1** shows the location of the sampling sites. The sampling sites were away from roads and human activities. Five points were randomly arranged at each sampling site to collect topsoil at a depth of 15 cm; two points were at least 500 m apart. Kosa particles collected at the five points were then mixed and sealed in a polytetrafluoroethylene (PTFE) bottle and stored at -20°C away from light.
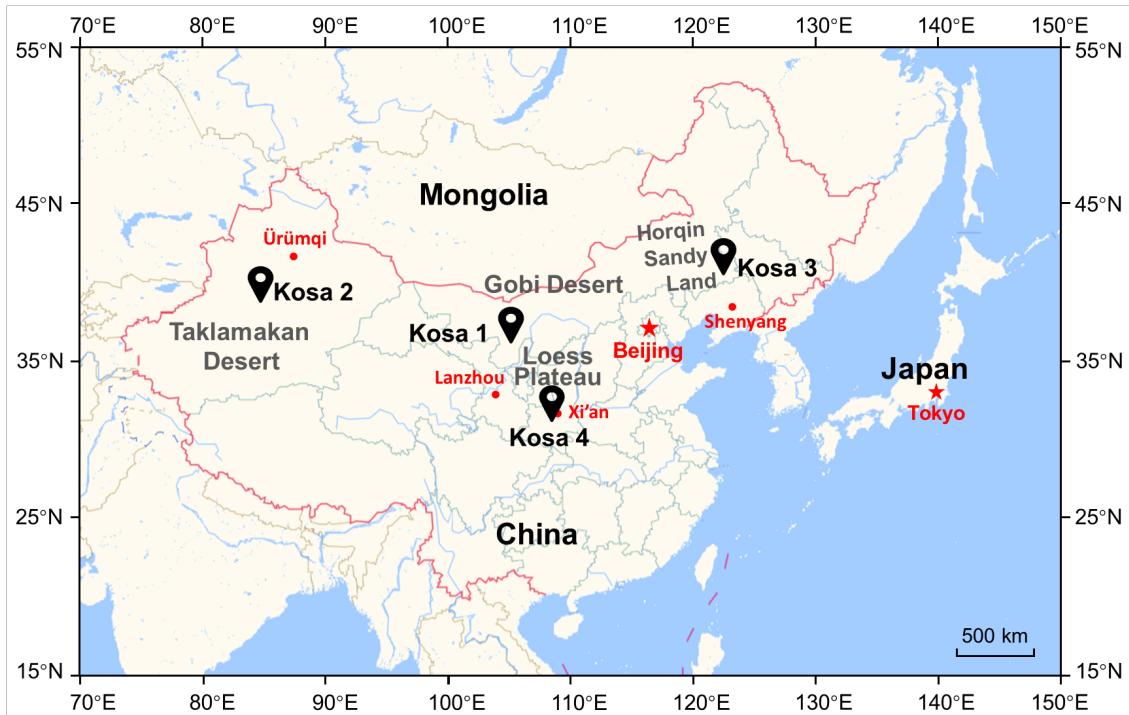
Fig. 1-1. Locations of the geographic origin of Kosa samples. Sample Kosa 1 was collected from the Gobi Desert (105.4°E, 38.5°N, Inner Mongolia, China), Kosa 2 was from the Taklimakan Desert (84.3°E, 40.2°N, Xinjiang, China), Kosa 3 was from the Horqin Sandy Land (122.3°E, 43.0°N, Inner Mongolia, China) and Kosa 4 was from the Loess Plateau (108.9°E, 34.5°N, Shaanxi, China).

2.3 Physical properties measurement

The physical properties of the Kosa particles, including size distribution, specific surface area, and porosity, were measured with the assistance of an analyzing agency (Shimadzu Techno-Research, Inc., Kyoto, Japan). The laser particle size analyzer (Shimadzu SALD-2300) was employed to measure the particle size of the Kosa samples. The multipoint Brunauer-Emmett-Teller (BET) method, i.e. the nitrogen adsorption method (Shimadzu ASAP2400), was applied to determine the specific surface area, total pore volume, and pore size of each Kosa sample.

2.4 Chemical composition measurement

Metallic elements

Ten grams of each Kosa sample was placed in a PTFE digestion high-pressure tank with 9 mL of mixed acid (HNO_3/HF/H_2O_2, 5:3:1, v/v). The mixture was treated by microwave digestion for 30 min and cooled to room temperature. The digestive solution was then concentrated by heating at 220°C to 0.5 mL and diluted to 50 mL with 2% HNO_3. Fifteen metallic elements, including Al, Fe, Ca, Na, potassium (K), Mg, Ti, phosphorus (P), Mn, barium (Ba), strontium (Sr), nickel (Ni), zinc (Zn), Cu, and scandium (Sc), were determined by using a high-resolution inductively coupled plasma mass spectrometer (Thermo X series II, Thermo Fisher Scientific K.K., Tokyo, Japan) and quantified by internal standards. The recoveries were in the range of 95% to 105%.

The elemental compositions of the reference samples CJ 1 and CJ 2 were treated and detected simultaneously. The pretreatment and detection were repeated for three times of each Kosa sample, and for six times of each reference sample. Method calibration was performed by comparing the measured values with the reference values of CJ 1 and CJ 2. Both the measured values of CJ 1 and CJ 2 samples were linearly correlated with the

corresponding reference values, and the determining coefficient (R^2) was 0.9996 and 0.9995, respectively.

Water-soluble inorganic ions

Ten grams of each Kosa sample were placed in a glass beaker with 50 mL ultrapure water. After standing at room temperature for 10 min, the water-soluble inorganic ions were extracted twice by ultrasonic extraction for 20 min. The mixture was then moved to a PTFE centrifuge tube and centrifuged at 3500 rpm for 15 min to precipitate Kosa particles. After that, 1 mL of the supernatant was diluted to 5 mL with ultrapure water. Prior to analysis, all the treated samples were filtered through a micropore membrane (Millex®-HP, pore size 0.45 μm, Merck KGaA Darmstadt, Germany).

Nine water-soluble inorganic ions, including Na^+, ammonium ion (NH_4^+), K^+, Ca^{2+}, Mg^{2+}, fluoride ion (F^-), Cl^-, NO_3^-, and SO_4^{2-}, were determined by ion chromatography (IC). The IC system (883 Basic IC plus, Metrohm, Herisau, Switzerland) consisted of analysis columns, a suppressed conductivity detector and an infusion pump (Metrohm, Herisau, Switzerland). A separation column (Shonex IC YK-421, 250 mm × 4.0 mm i.d., Showa Denko K. K., Tokyo, Japan), and a guard column (Shonex IC YK-G, 50 mm × 4.0 mm i.d., Showa Denko K. K., Tokyo, Japan) were applied to separate cations. A separation column (Shonex IC SI-90-4E, 250 mm × 4.0 mm i.d., Showa Denko K. K., Tokyo, Japan), a guard column (Shonex IC SI-90-G, 50 mm × 4.0 mm i.d., Showa Denko K. K., Tokyo, Japan), and a column oven (CTO-10ASVP, Shimadzu Inc., Kyoto, Japan) were applied to separate anions. The eluent for analyzing cations was 1.7 mM HNO_3 and 0.7 mM 2, 6-pyridinedicarboxylic acid solution. The eluent for analyzing anions was 3.2 mM Na_2CO_3 and 1.0 mM $NaHCO_3$ solutions.

The detection and quantification limits were calculated as three and ten times the signal-to-noise ratio, respectively. The detection limits of Na^+, NH_4^+, K^+, Ca^{2+}, Mg^{2+}, F^-, Cl^-, NO_3^-,

and SO_4^{2-} were 0.055, 0.101, 0.097, 0.125, 0.222, 0.003, 0.034, 0.074, and 0.041 mg L^{-1}, respectively. The quantification limits of Na^+, NH_4^+, K^+, Ca^{2+}, Mg^{2+}, F^-, Cl^-, NO_3^-, and SO_4^{2-} were 0.184, 0.336, 0.323, 0.416, 0.741, 0.009, 0.114, 0.246, and 0.137 mg L^{-1}, respectively. The standard curves were linear with all the R^2 greater than 0.995. The recoveries were in the range of 85% to 110%.

3 Results and discussion

3.1 Physical properties of different Kosa particles

Table 1-1 presents the average of the particle size, specific surface area, total pore volume, and pore size of the Kosa samples collected from different deserts. The average particle size of the Kosa 1 to 3 samples was similar, ranging from 191 to 263 μm. The average particle size of the Kosa 4 sample was 12.7 μm, which was much smaller than the other three Kosa samples. In contrast, the specific surface area and total pore volume of the Kosa 4 sample were the largest, at 32.8 m^2 g^{-1} and 52.0 μg L^{-1}, respectively, which were dozens of times those of the Kosa 1 to 3 samples. The average pore size of the four Kosa samples ranged from 3.78 to 7.13 nm. According to the recommendations of the International Union of Pure and Applied Chemistry (McCusker et al., 2001), these four Kosa samples can be classified into mesoporous materials (pore size between 2 to 50 nm) by pore size.

Table 1-1. Physical properties of different Kosa samples.

Kosa	Average diameter (μm)	Specific surface area (BET) (m^2 g^{-1})	Total pore volume (μL g^{-1})	Average pore diameter (nm)
1	222	3.02	2.85	3.78
2	191	1.73	3.09	7.13
3	263	2.20	2.66	4.83
4	12.7	32.8	52.0	6.35

3.2 Metallic elements of different Kosa particles

Table 1-2 shows the composition of metallic elements of the four Kosa particles. Generally, silicon (Si) is the most abundant metallic element in natural mineral dust and crust (Jeong, 2020; Shen et al., 2007). In the soil samples collected in arid and semi-arid areas in East Asia, Si had the highest mass fraction, at 25-35%, followed by Al (4.3-7.5%), Fe (1.2-4.1%), and Ca (0.6-8.5%) (Nishikawa et al., 2018). Due to insufficient detection conditions, the content of Si in the Kosa particles was not obtained in this study. As shown in **Table 1-2**, the metallic elements in the four Kosa particles were rich in crustal elements (such as Al, Fe, Ca, Na, and K), while the content of transition metals (such as Ti, Mn, Ni, Zn, and Cu) was relatively low.

The mass fraction of each metallic element in the Kosa particles was comparable to the previously reported desert soil of the corresponding source area (**Table 1-3**; Nishikawa et al., 2018), showing significant regional differences. The crustal elements of Kosa 1 and Kosa 3 particles were more abundant with Al and K, while the main crustal elements of Kosa 2 and Kosa 4 particles were Al and Ca, and Al and Fe, respectively. Compared with other transition metals, Ti and Mn were more abundant in the four Kosa particles. In addition, Cu and Zn were the main transition metals in anthropogenic particles (Sun et al., 2005) but were present at trace levels in the four Kosa particles. Therefore, the Kosa events increased the content of crustal elements in atmospheric particles in downwind areas, while reduced the content of transition metals associated with human activities (Dong et al., 2019; Wang et al., 2018).

Table 1-2. Composition of metallic elements of different Kosa samples.

Element	Unit	Kosa 1		Kosa 2		Kosa 3		Kosa 4	
		Mean	SD	Mean	SD	Mean	SD	Mean	SD
Al	(%)	4.82	0.32	5.48	0.18	2.80	0.34	7.48	0.17
Fe	(%)	0.88	0.09	1.66	0.03	0.29	0.10	3.66	0.10
Ca	(%)	0.54	0.03	6.32	0.42	0.18	0.04	0.67	0.05
Na	(%)	1.62	0.13	1.81	0.10	0.56	0.06	0.76	0.02
K	(%)	2.28	0.18	1.93	0.03	2.11	0.36	2.12	0.05
Mg	(%)	0.39	0.03	1.09	0.04	0.04	0.03	0.98	0.03
Ti	(%)	0.12	0.03	0.18	0.03	0.04	0.03	0.41	0.01
P	(μg g^{-1})	1630	478	1270	135	749	83.7	1100	93.8
Mn	(μg g^{-1})	151	24.7	366	38.7	65.6	34.2	745	49.0
Ba	(μg g^{-1})	697	62.2	632	62.6	501	45.8	501	13.0
Sr	(μg g^{-1})	151	9.01	270	14.0	92.7	11.1	110	1.90
Ni	(μg g^{-1})	14.2	2.94	19.0	1.59	2.77	0.08	40.9	0.95
Zn	(μg g^{-1})	30.8	6.18	49.0	8.35	14.3	5.90	85.3	11.1
Cu	(μg g^{-1})	10.9	1.62	12.5	1.02	3.33	0.77	31.5	1.31
Sc	(μg g^{-1})	3.00	0.60	5.76	0.52	0.35	0.32	12.8	0.33
Total	(%)	10.9	0.87	18.7	0.86	6.16	0.98	16.3	0.45

The metallic elements are arranged in the order of terrestrial abundance of elements, refer to https://www.daviddarling.info/encyclopedia/E/elterr.html, accessed on 24th Jun. 2020.

Abbreviations: standard deviation (SD), aluminum (Al), iron (Fe), calcium (Ca), sodium (Na), potassium (K), magnesium (Mg), titanium (Ti), phosphorus (P), manganese (Mn), barium (Ba), strontium (Sr), nickel (Ni), zinc (Zn), copper (Cu), scandium (Sc).

Table 1-3. Elemental composition of topsoil in different dust sources (Nishikawa et al., 2018).

Element	Unit	Gobi Desert [a]	Taklimakan Desert [b]	Horqin Sandy Land [c]	Loess Plateau [d]
Si [e]	(%)	27.8 - 33.5	25.5 - 29.4	33.1 - 34.9	26.3 - 30.1
Al	(%)	6.11 - 7.49	5.02 - 5.74	4.31 - 6.22	5.66 - 6.54
Fe	(%)	2.06 - 4.10	1.84 - 2.71	1.23 - 1.76	2.57 - 3.07
Ca	(%)	0.90 - 4.02	6.05 - 8.48	0.59 - 0.99	3.94 - 6.79
Na	(%)	1.33 - 2.57	1.42 - 1.68	1.67 - 1.80	1.15 - 1.40
K	(%)	2.13 - 2.81	1.51 - 1.87	2.38 - 2.44	1.63 - 1.93
Mg	(%)	0.47 - 2.12	1.12 - 1.63	0.26 - 0.35	0.99 - 1.55
Ti	(%)	0.405 - 0.727	0.240 - 0.426	0.333 - 0.410	0.329 - 0.441
P	(μg g^{-1})	248 - 1114	525 - 1047	141 - 299	462 - 1054
Mn	(μg g^{-1})	514 - 933	433 - 627	302 - 466	459 - 666
Ba	(μg g^{-1})	512 - 610	442 - 531	584 - 629	450 - 510
Sr	(μg g^{-1})	215 - 296	250 - 298	199 - 203	173 - 274
Ni	(μg g^{-1})	N.A. [f]	N.A.	N.A.	N.A.
Zn	(μg g^{-1})	27 - 92	24 - 53	20 - 34	50 - 66
Cu	(μg g^{-1})	7 - 45	10 - 16	6 - 8	17 - 23
Sc	(μg g^{-1})	7 - 15	6 - 10	4 - 5	9 - 11

[a] Gobi Desert region (20 sites): 41.83°N, 114.00°E; 42.33°N, 113.83°E; 42.38°N, 103.47°E; 42.78°N, 103.50°E; 43.09°N, 106.33°E; 43.22°N, 107.09°E; 43.47°N, 104.65°E; 43.59°N, 112.00°E; 43.72°N, 111.87°E; 43.77°N, 103.98°E; 43.77°N, 104.02°E; 43.83°N, 113.75°E; 44.05°N, 111.33°E; 44.11°N, 103.57°E; 44.25°N, 111.07°E; 44.93°N, 110.60°E; 45.13°N, 109.94°E; 45.83°N, 106.23°E; 45.99°N, 108.79°E; 46.32°N, 108.37°E. [b] Taklimakan Desert region (7 sites): 37.04°N, 81.00°E; 37.09°N, 80.10°E; 37.24°N, 82.77°E; 37.63°N, 78.12°E; 38.02°N, 77.40°E; 39.46°N, 83.90°E; 41.86°N, 86.26°E. [c] Sites near Horqin Sandy Land (2 sites): 42.17°N, 122.72°E; 43.29°N, 122.24°E. [d] Loess Plateau region (7 sites): 35.58°N, 109.26°E; 35.70°N, 105.10°E; 35.82°N, 109.47°E; 37.81°N, 110.34°E; 37.90°N, 112.60°E; 40.33°N, 113.50°E; 40.60°N, 115.10°E. [e] Silicon. [f] Not available.

3.3 Water-soluble inorganic ions of different Kosa particles

Table 1-4 shows the mass fraction of each water-soluble inorganic ion on the surface of different Kosa particles. Consistent with the regional difference in metallic elements, the ionic composition of Kosa particles varied greatly with geographical origins. The mass fraction of nine water-soluble inorganic ions in the Kosa 2 sample was the highest (665 μg g^{-1}), followed by the samples Kosa 1 (324 μg g^{-1}) and Kosa 4 (290 μg g^{-1}), and the lowest in the Kosa 3 sample (26.7 μg g^{-1}). In the Kosa 1 and Kosa 2 particles, Na^+ and Cl^- were the most abundant ions, followed by SO_4^{2-}. These results were consistent with the ionic composition of the Kosa particles in the Gobi Desert and Taklimakan Desert in the literature (Tang et al., 2019), which were related to their salt playa origin (Wang et al., 2012; Wu et al., 2012). The main ionic components in the Kosa 3 and Kosa 4 particles were Ca^{2+}, SO_4^{2-} and NO_3^-. Based on the composition of deliquescent salts (NaCl, Na$_2$SO$_4$, and Ca(NO$_3$)$_2$) (Tang et al., 2016), these four Kosa particles could attract water from the atmosphere.

Table 1-4. Mass fraction of water-soluble inorganic ions of different Kosa samples.

Ion (μg g^{-1})	Kosa 1	Kosa 2	Kosa 3	Kosa 4
Na^+	136	222	1.24	19.7
NH_4^+	N.D.	0.28	2.05	0.24
K^+	6.35	13.7	3.94	3.29
Ca^{2+}	3.44	29.4	8.55	37.2
Mg^{2+}	2.77	4.79	1.50	25.4
F^-	1.18	1.16	0.37	4.30
Cl^-	121	270	0.32	5.08
NO_3^-	8.97	22.6	4.54	41.5
SO_4^{2-}	44.0	101	4.17	153
Total	324	665	26.7	290

Abbreviations: not detected (N.D.), sodium ion (Na^+), ammonium (NH_4^+), potassium ion (K^+), calcium ion (Ca^{2+}), magnesian ion (Mg^{2+}), fluorinion (F^-), chloridion (Cl^-), nitrate ion (NO_3^-), sulfate ion (SO_4^{2-}).

4 Conclusion

Kosa particles collected from the Gobi Desert, Taklimakan Desert, Horqin Sandy Land, and Loess Plateau had different physical properties and chemical compositions. Compared to the other three Kosa samples, the Kosa 4 sample from the Loess Plateau had the smallest particle size and the highest specific surface area and total pore volume. The contents of the metallic elements and water-soluble inorganic ions of the four Kosa particles were comparable to the previously reported desert soils from the corresponding source areas, showing large regional differences. The four Kosa samples were characterized by a high content of crustal elements and a low level of transition metal elements, whereas the mass fraction of each element varied largely. Besides, these four Kosa samples had different compositions on water-soluble inorganic ions, but the main components all were deliquescent salts. These differences in physical property and chemical composition may affect the role of Kosa particles of different origins in the atmospheric process.

Chapter 2. Adsorption of different Kosa particles to naphthalene

1 Introduction

During the displacement and transport, the Kosa particles collide with gas molecules in the atmosphere, triggering physical and chemical adsorption on the particle surface (Fairlie et al., 2018; Kim et al., 2012b). The current interest mainly lies in the heterogeneous uptake of inorganic gas by minerals, which has an acid-base preference (Yang et al., 2018; Zhou et al., 2015). Alkaline minerals, such as MgO and CaO, have higher adsorption efficiency for acid gases, such as SO_2 and NO_2, whereas the acid sites on the particle surface tend to associate with the basic gas NH_3 (Yang et al., 2018). These gas molecules adsorbed on the particle surface are then converted through electron transfer into dissolved compounds, i.e. SO_4^{2-}, NO_3^-, and NH_4^+, which are the main components of secondary inorganic aerosols (He et al., 2015).

The adsorption of gaseous organic molecules by mineral particles is in different patterns. The mineral particles adsorb weakly ionized organic molecules (such as isopropanol) through intermolecular interactions, i.e. physical adsorption (Romanias et al., 2016; Zeineddine et al., 2018), while the interaction between gaseous organic acids and mineral particles involves both physical and chemical adsorption. For example, formic and acetic acids bind to the mineral particles via hydrogen bonding and then react with basic groups on the surface, such as hydroxyl (OH) group and calcium carbonate ($CaCO_3$) (Wang et al., 2020). Different from alcohols and acids, PAHs are nonpolar organic molecules. Studies have shown that sandy soil particles adsorb PAHs through physical adsorption (Ngueleu et al., 2018), while chemical bonding is dominated in the adsorption between PAHs and clay minerals containing exchangeable cations or metal-modified minerals (Meleshyn and

20

Tunega, 2011; Saeedi et al., 2018). However, compared with the polar and hydrophilic surface of mineral particles, PAH molecules tend to be associated with the nonpolar surface or lipid components of other atmospheric particles (Cochran et al., 2016; Zhang et al., 2016).

Physical adsorption primarily depends on the specific surface area and total pore volume of mineral particles, whereas chemical adsorption is related to the surface groups of particles (Huang et al., 2017; Marquès et al., 2017; Yakout et al., 2013). In addition, the water layer on the particle surface can weaken the physical adsorption of organic molecules (Zeineddine et al., 2018) and enhance the chemical adsorption of inorganic gases and ionizable organic molecules (Wang et al., 2020). Due to the hydrophobicity of PAHs, the water layer formed on the mineral particles could produce a negative influence on the physical and chemical adsorption of PAHs (Haro et al., 2011; Li et al., 2018).

The four Kosa particles in this study have different physical properties and chemical compositions, which may lead to different adsorption of PAHs. Therefore, batch adsorption experiments were performed with Nap as the probe PAH to clarify the adsorption capacity of different Kosa particles to PAHs.

2 Materials and methods

2.1 Chemicals

Nap (99%), hydrochloric acid (HCl), sulfuric acid (H_2SO_4), and HNO_3 were provided by Wako Pure Chemical Industries, Ltd. (Osaka, Japan). All chemicals used in this study were of analytical reagent grade.

2.2 Preparation

Because of the poor solubility of Nap, the aqueous solution of Nap at various concentrations were prepared with methanol as a co-solvent. The volume fraction of methanol in the aqueous solution was 5%. First, a certain amount of Nap was dissolved in the methanol on a magnetic stirrer (Pasolina Mini Stirrer, CT-MINI, As One Co., Osaka, Japan) at room temperature. Then it was diluted by slowly adding ultrapure water with the stirring continues. After ultrasonic degassing, the Nap solution was stored in an amber bottle at room temperature away from light.

Kosa particles were treated before the experiments. First, organic contaminants were extracted from each Kosa sample by ultrasonic waves with methanol. Then, the extracts were analyzed by high-performance liquid chromatography (HPLC) coupled with ultraviolet (UV) detection (SPD-20A series, Shimadzu Inc., Kyoto, Japan). The background level of PAHs of the four Kosa samples was negligible because it was below the detection limit of PAHs. After air drying, the remaining methanol on the particles was evaporated by heating at 100°C for 2 h. Each Kosa sample was stored in a clean PTFE bottle after cooling to room temperature.

2.3 Batch adsorption experiments

The setup of the adsorption experiment is described in **Fig. 2-1**. In the experiment, a certain amount of each Kosa sample was mixed with 40.0 mL of Nap solution in a 100 mL conical flask closed with a glass stopper to avoid evaporation. Then, 1.0 mL of the solution was taken out for HPLC analysis. The conical flasks were covered with aluminum foil to protect from light and were placed in a thermostatic shaker water bath at 20°C for 24 h. The blank control group (excluding Kosa particles) was carried out simultaneously.
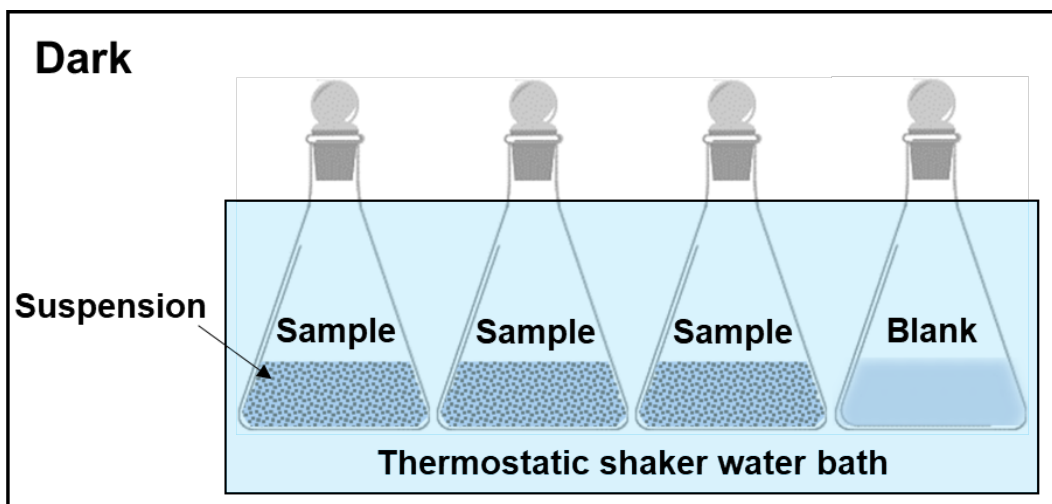
Fig. 2-1. Schematic diagram of the adsorption experiment. The suspension is the mixture of Kosa particles and Nap solution. The blank sample contains no Kosa sample.

After 24-h shaking, 1.0 mL of the solution was transferred to an amber vial for HPLC analysis. Then, 35.0 mL of the solution was removed from the conical flask. The residual solution (3.0 mL) and Kosa particles in the conical flask were extracted twice through ultrasonication with 10.0 mL methanol. After that, the solution was centrifuged at 3500 rpm for 15 min to precipitate Kosa particles, and 20 μL of the supernatant was injected into the HPLC system for quantitative analysis. The quantity of Nap (m) associated with Kosa particles was estimated by **Eq. 2-1**.

$$m = m_2 - 3/39 \times m_1 \hspace{5cm} \textbf{(Eq. 2-1)}$$

where m_1 is the quantity of Nap in the solution after shaking, mg; m_2 is the quantity of Nap in the mixture of residual solution and Kosa particles, mg; 39 is the volume of the solution for shaking, mL; 3 is the volume of the residual solution, mL.

The batch adsorption experiment under acid conditions was carried out following the same protocol. During the transportation and deposition of Kosa, it would neutralize the acidic substances in the air in downwind areas and change the acidity of the local precipitation (Wang et al., 2002). The precipitation in Chinese, Korean and Japanese cities showed an obvious trend from acidic (pH = 4.0-5.0) to slightly acidic (pH = 6.0-7.0) during Kosa events (Liu et al., 2013; Wang et al., 2002; Yang et al., 2004). Therefore, the pH of the aqueous solution was adjusted to 4.5 in the batch adsorption experiment under acid conditions. Three common acids in the atmosphere, HCl, H_2SO_4, and HNO_3, were separately added to the aqueous solution of Nap to adjust the acidity to pH = 4.5. The pH of the aqueous solution was measured by a pH meter (F-70 series, Horiba Ltd., Kyoto, Japan).

The adsorption experiments employed the Kosa 1 to Kosa 3 samples were performed in two mass groups (1.5 g and 3.0 g). The adsorption experiments employed the Kosa 4 sample were performed in eleven mass groups (7.5 mg, 10 mg, 12.5 mg, 15 mg, 30 mg, 75 mg, 0.37 g, 0.75 g, 1.5 g, 3.0 g, and 4.5 g). Each Kosa group and blank group contained four parallel

samples, with the relative standard deviation (RSD) of the Nap concentration less than 5%. The concentration of Nap solutions was about 14.0 mg L^{-1}, in the range from 13.07 mg L^{-1} to 14.38 mg L^{-1}. The adsorption experiments of 10 mg KOSA 4 sample were performed in Nap solution at different concentrations (3.11 mg L^{-1}, 7.13 mg L^{-1}, 8.55 mg L^{-1} and 13.8 mg L^{-1}) to determine the adsorption isotherm. Since the loss of Nap might be caused by adsorption on the inner wall of conical flask, the adsorption data of each Kosa group were shown as the average after deducting the blank.

2.4 Chemical analysis

An HPLC equipped with a reversed-phase column (Inertsil ODS-P, 4.6 i.d. $\times$ 250 mm, GL Sciences Inc., Tokyo, Japan) and a UV detector (SPD-20A series, Shimadzu Inc., Kyoto, Japan) was used in quantitative analysis of Nap and the extracts of Kosa samples. The mobile phase was a mixture of acetonitrile/water (9:11, v/v) at a flow rate of 1 mL min^{-1}. The wavelength used in the UV detector was 254 nm. Prior to analysis, all the samples were filtered through the HLC-DISK membrane (pore size 0.45 μm, Kanto Chemical Co., Tokyo, Japan). The recovery of Nap was 99%. The detection and quantification limits of Nap were 69.0 ng L^{-1} and 230 ng L^{-1}, respectively. The standard curve was linear, with the R^2 of 0.9999.

2.5 Adsorption isotherm model

The Langmuir adsorption isotherm model describes the physical adsorption of monolayers and is widely used to estimate the adsorption performance of mineral materials (Chang et al., 2004). In this work, the adsorption of Kosa particles for Nap was described with the linear algorithm of the Langmuir adsorption isotherm model (**Eq. 2-2**). The adsorption curve was then calculated by the Langmuir adsorption isothermal equation (**Eq. 2-3**).

$$1/Q = 1/k_{ad}Q_\mathrm{m} \cdot 1/C + 1/Q_\mathrm{m} \qquad \text{(Eq. 2-2)}$$

$$Q_\mathrm{e} = \frac{k_{ad}Q_\mathrm{m}C_\mathrm{e}}{1+k_{ad}C_\mathrm{e}} \qquad \text{(Eq. 2-3)}$$

where Q is the amount of Nap adsorbed on the Kosa particles, mg g^{-1}; Q_m is the maximum absorption capacity of Nap on the Kosa particles, mg g^{-1}; Q_e is the equilibrium adsorption capacity of Nap on the Kosa particles, mg g^{-1}; k_{ad} is the adsorption rate constant, L mg^{-1}; C is the concentration of the aqueous solution of Nap, mg L^{-1}; and C_e is the concentration of Nap solution at adsorption equilibrium, mg L^{-1}.

3 Results

3.1 Adsorption of naphthalene by different Kosa particles

Fig. 2-2 presents the adsorption of Nap by different Kosa particles of 1.5 g and 3.0 g in the aqueous solution. At the same Kosa mass, the amount of Nap adsorbed on the Kosa 4 particles was several times higher than that on the other three Kosa particles. Moreover, the Nap adsorbed by the Kosa 4 particles increased with the Kosa mass. However, there were no obvious dependence between the mass of Kosa 1 to 3 particles and the adsorption of Nap.

Due to the obvious adsorption on the Kosa 4 particles, the adsorption of Nap by the Kosa 4 particles with a mass of 7.5 mg to 3.0 g was observed under the same conditions, and the results were showed in **Fig. 2-3**. The adsorption of Nap on the Kosa 4 particles displayed an approximate logarithmic trend as the Kosa mass increased ($R^2 = 0.785$); additionally, the adsorption amount of Nap on the Kosa 4 particles increased more rapidly from 7.5 mg to 30 mg.
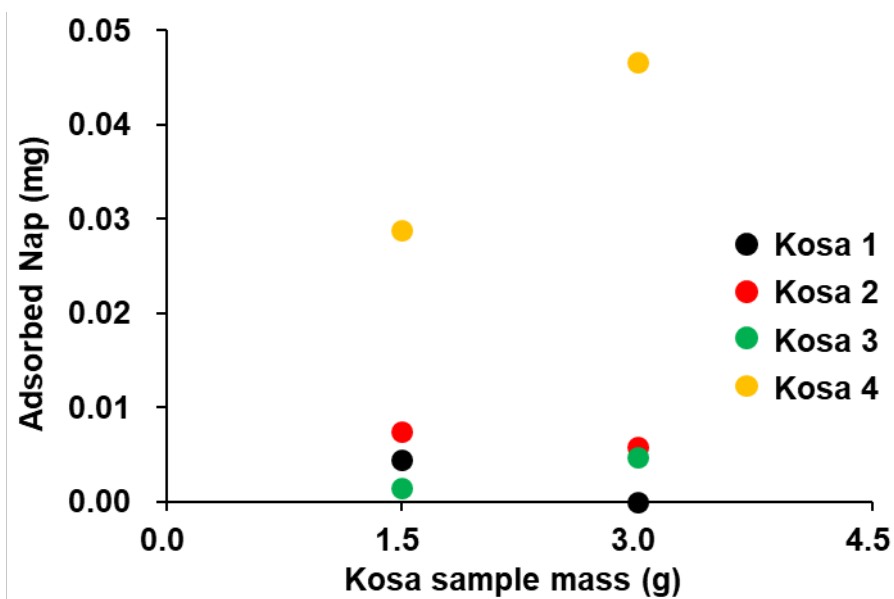
Fig. 2-2. The adsorption of Nap on different Kosa samples in the aqueous solution of Nap (14 mg L^{-1}).
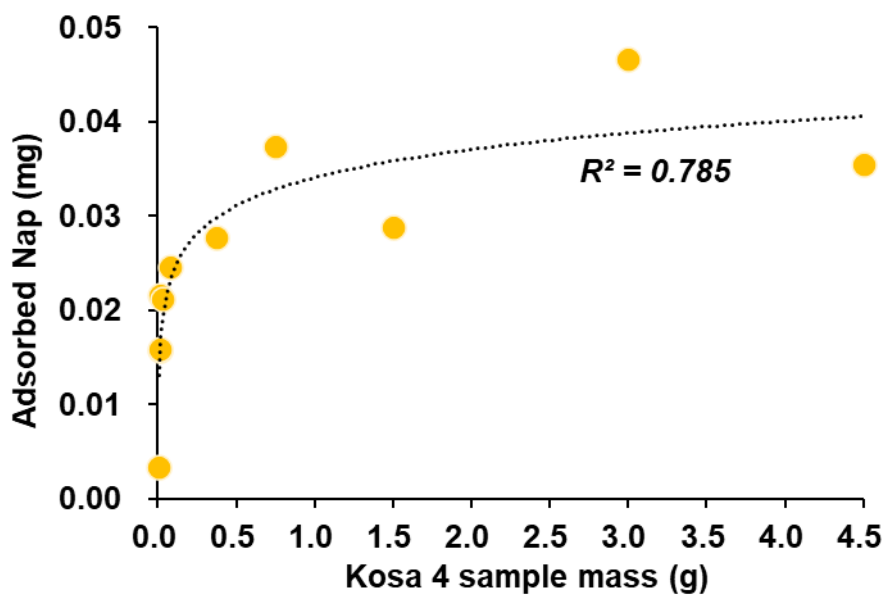
Fig. 2-3. The adsorption of Nap on the Kosa 4 sample in the aqueous solution of Nap (14 mg/L). R^2 is the determination coefficient of the trend line.

The adsorption amount of Nap on 10 mg of Kosa 4 particles in the acid solutions was shown in **Table 2-1**. After a 24-h adsorption experiment, the loss of Nap in the acid solution containing Kosa 4 particles was comparable to that containing no Kosa, which was independent of the acid type. However, under acid-free conditions, the loss of Nap in the sample containing Kosa 4 particles was significantly higher than that in the blank sample (t-test; $p < 0.01$, $n = 4$). This difference indicates that the loss of Nap in the acidic solution was related to the same process as in the blank, such as the adsorption of the inner wall of the container, but not to the adsorption by the Kosa 4 particles.

Table 2-1. Reduction in Nap after 24-h adsorption experiment under acidic and acid-free conditions.

Aicd	HCl	H_2SO_4	HNO_3	Acid-free
Kosa 4 sample	$-$ [a]	(0.014 ± 0.007) mg	(0.032 ± 0.004) mg	(0.096 ± 0.006) mg
Blank	$-$	(0.016 ± 0.006) mg	(0.032 ± 0.007) mg	(0.080 ± 0.006) mg

[a] No reduction.

3.2 Simulation with adsorption model

The adsorption of Nap by the Kosa 4 particles was estimated by performing the batch experiment in Nap solution at various concentrations. As shown in **Fig. 2-4a**, the experimental data were well represented by the linear form of the Langmuir adsorption isotherm model ($R^2 = 0.973$). This result suggests that the adsorption of Nap by the Kosa 4 particles was a monolayer physical adsorption, which was driven by the molecular interaction between the particle surface and Nap (Qian et al., 2011).

In **Fig. 2-4b**, the adsorption of Nap by the Kosa 4 particles was simulated by the Langmuir adsorption isotherm model. The relevant parameters were given in **Table 2-2**. With the increase in Nap concentration, the adsorption capacity of the Kosa 4 particles to Nap increased rapidly at the beginning, then gradually stabilized and approached the maximum adsorption capacity (2.87 mg g^{-1}). This was because the adsorption of Nap by the Kosa 4 particles gradually saturated, as the adsorption sites on the surface were occupied (Qian et al., 2011). However, due to the poor water-solubility of Nap, Kosa 4 particles could not reach the maximum adsorption capacity for Nap. At room temperature, the concentration of Nap in saturated aqueous solution is about 31 mg L^{-1}. Under this condition, the adsorption capacity of the Kosa 4 particles to Nap was 1.66 mg g^{-1} (**Fig. 2-4b**), which was much lower than that of the zeolites (a kind of microporous mineral) to Nap (31.23 mg g^{-1}; Chang et al., 2004). This gap indicates the relatively weak adsorption of Nap by the Kosa 4 particles.
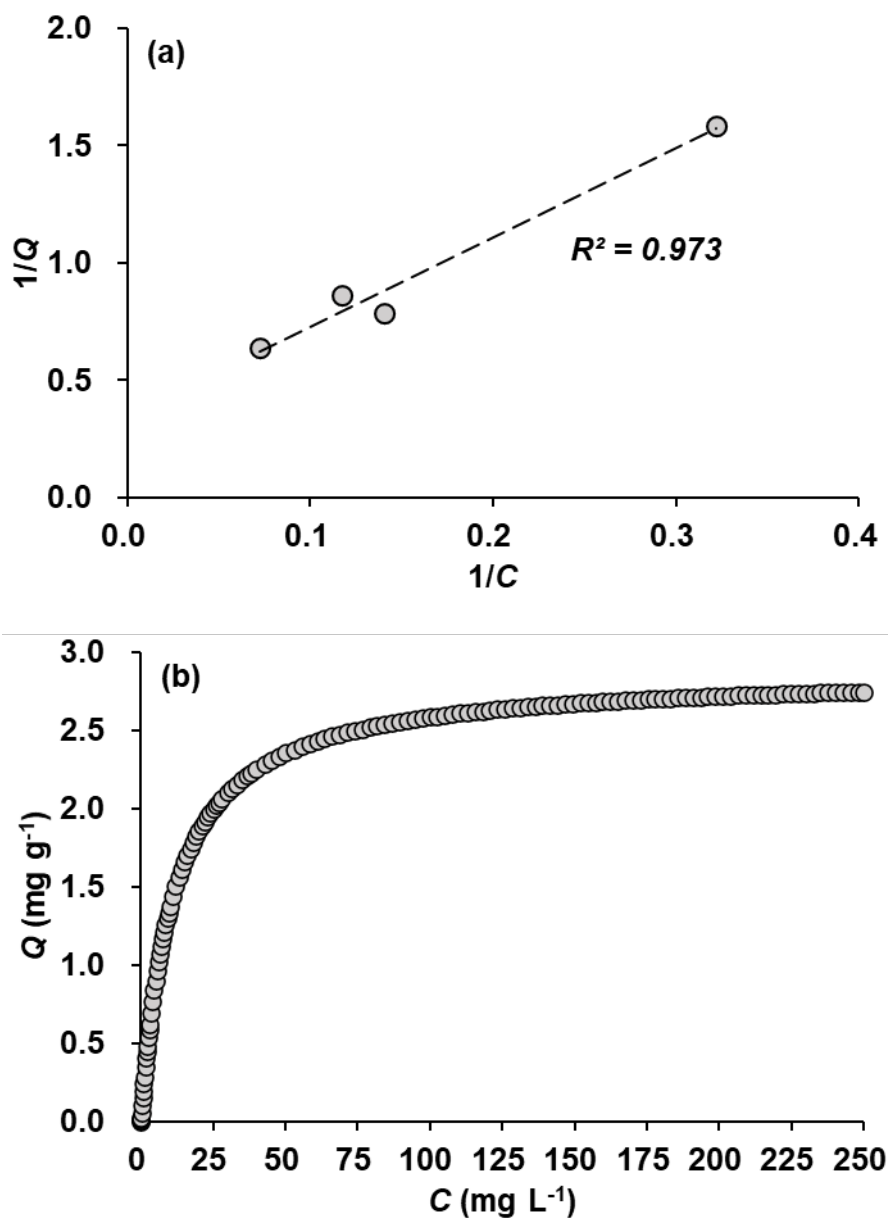
Fig. 2-4. The adsorption of Nap on 10 mg of the Kosa 4 sample fitted by (a) the linear form of Langmuir adsorption isotherm, (b) the Langmuir adsorption isotherm. C is the concentration of Nap aqueous solution, mg L^{-1}; Q is the adsorption amount of Nap per unit quality of the Kosa 4 sample, mg g^{-1}.

Table 2-2. Adsorption data and the Langmuir isotherm parameters for Nap on the Kosa 4 sample.

C	Q	1/C	1/Q	k_{ad}	Q_m
3.11	0.631	0.322	1.58	0.0918	2.87
7.13	1.27	0.140	0.785		
8.55	1.16	0.117	0.860		
13.8	1.56	0.0725	0.640		

C is the concentration of Nap aqueous solution, mg L^{-1}; Q is the adsorption amount of Nap per unit quality of the Kosa 4 sample, mg g^{-1}; k_{ad} is the adsorption equilibrium constant, L mg^{-1}; Q_m is the maximum adsorption, mg g^{-1}.

4 Discussion

The adsorption properties of solid substrates are related to surface properties and porosity (Huang et al., 2017; Yakout et al., 2013). Compared with the other three Kosa particles, the Kosa 4 particles had the largest specific surface area, which suggests that the Kosa 4 particles can provide more adsorption sites at the same mass. In addition, the pore types of the four Kosa particles were consistent, thus the larger total pore volume of the Kosa 4 particles indicates a higher adsorption capacity. However, the adsorption capacity of the Kosa 4 particles to Nap was much lower than that of the microporous zeolites (Chang et al., 2004), indicating that microporous minerals could bind Nap more effectively than Kosa particles.

The composition of the solid substrate and the surface functional groups can influence the adsorption selectivity (Smol and Włodarczyk-Makuła, 2017). For example, activated carbon is a nonpolar carbonaceous material, which is more effective in adsorbing nonpolar organic molecules (Yakout et al., 2013); moreover, aliphatic groups have stronger adsorption affinity for PAHs than aromatic groups (Zhang et al., 2016); whereas silica gel and zeolite are composed of silica and aluminosilicates, respectively, and are more inclined to adsorb polar molecules (Chang et al., 2004; Vidal et al., 2011). Similar to silica gel and zeolite, Kosa particles are a mixture of various minerals and have polar surfaces. Therefore, Kosa particles have stronger adsorption selectivity for polar molecules in the atmosphere such as inorganic gases, than for nonpolar molecules such as Nap. Moreover, PAHs with higher molecular weight are more hydrophobic that are more difficult to be adsorbed by Kosa particles than Nap. In addition, based on the experimental results under acid conditions, the acidification of the surface of Kosa particles that can be caused by the uptake of SO_2 and NO_2, would make the adsorption of PAHs more insignificant.

In conclusion, among the four Kosa particles collected from typical deserts in East Asia, the Kosa 4 particles showed weak physical adsorption to Nap that was well represented by the Langmuir adsorption isothermal model. The Kosa particles collected from the Gobi Desert, Taklimakan Desert, and Horqin Sandy Land had no obvious adsorption to Nap. This might be because their specific surface area and total pore volume were much smaller than the Kosa 4 particles. In addition, the adsorption capacity of the Kosa 4 particles to Nap was much lower than that of zeolites under the same conditions. These results emphasize that Kosa particles could not compete with microporous minerals and nonpolar surfaces on the adsorption of PAHs, and the acidified Kosa particles were more disadvantaged. Therefore, Kosa particles are not considered to be a good carrier for PAH molecules in the atmosphere.

Chapter 3. Reaction of naphthalene in the saturated water layers of Kosa particles

1 Introduction

The atmospheric chemical processes of PAHs include gas phase and heterogeneous reactions involving OH and nitro (NO_3) radicals, oxygen (O_2), ozone (O_3), and NO_2, and photodegradation (Dang et al., 2014; Mmereki et al., 2004; Reyes et al., 2000; Ringuet et al., 2012; Shiraiwa et al., 2009; Zhang et al., 2011; Zhou and Wenger, 2013). Based on the reaction mechanisms calculated by the density functional theory and the rate constants obtained by laboratory research, the gas phase reaction initiated by the addition of OH radicals dominates the atmospheric reactions of PAHs (Dang et al., 2014; Gnanaprakasam et al., 2017; Ma et al., 2010; Qu et al., 2006).

Fig. 3-1 shows the different reaction pathways of Nap proposed by previous studies (Bunce and Zhu, 1995; Raja and Valsaraj, 2005; Sasaki et al., 1997; Vialaton et al., 1999). The main reaction pathways of 3- and 4-ring PAHs are consistent with Nap (Mmereki et al., 2004; Zhou and Wenger, 2013), while there are other alternative pathways for more complex PAHs (Jariyasopit et al., 2014; Marquès et al., 2017). Nevertheless, the mechanisms of these reactions are similar. As expressed by reactions (1), (5), (6), and (8), PAH molecules are excited by active oxidants or photons to produce PAH radicals (f) or the OH- or NO_3-adduct of PAHs (a or e). These intermediates then break down or undergo dehydrogenation or addition with other molecules, causing the formation of different products. The main products of Nap include oxygenated derivatives (such as α-naphthol (b) and 1, 4-naphthoquinone (g)), nitrated derivatives (such as 2-nitronaphthalene (d)), and ring-opening products (such as 2-formylcinnamaldehyde (c) and 1, 2-benzenedicarboxaldehyde (h)).
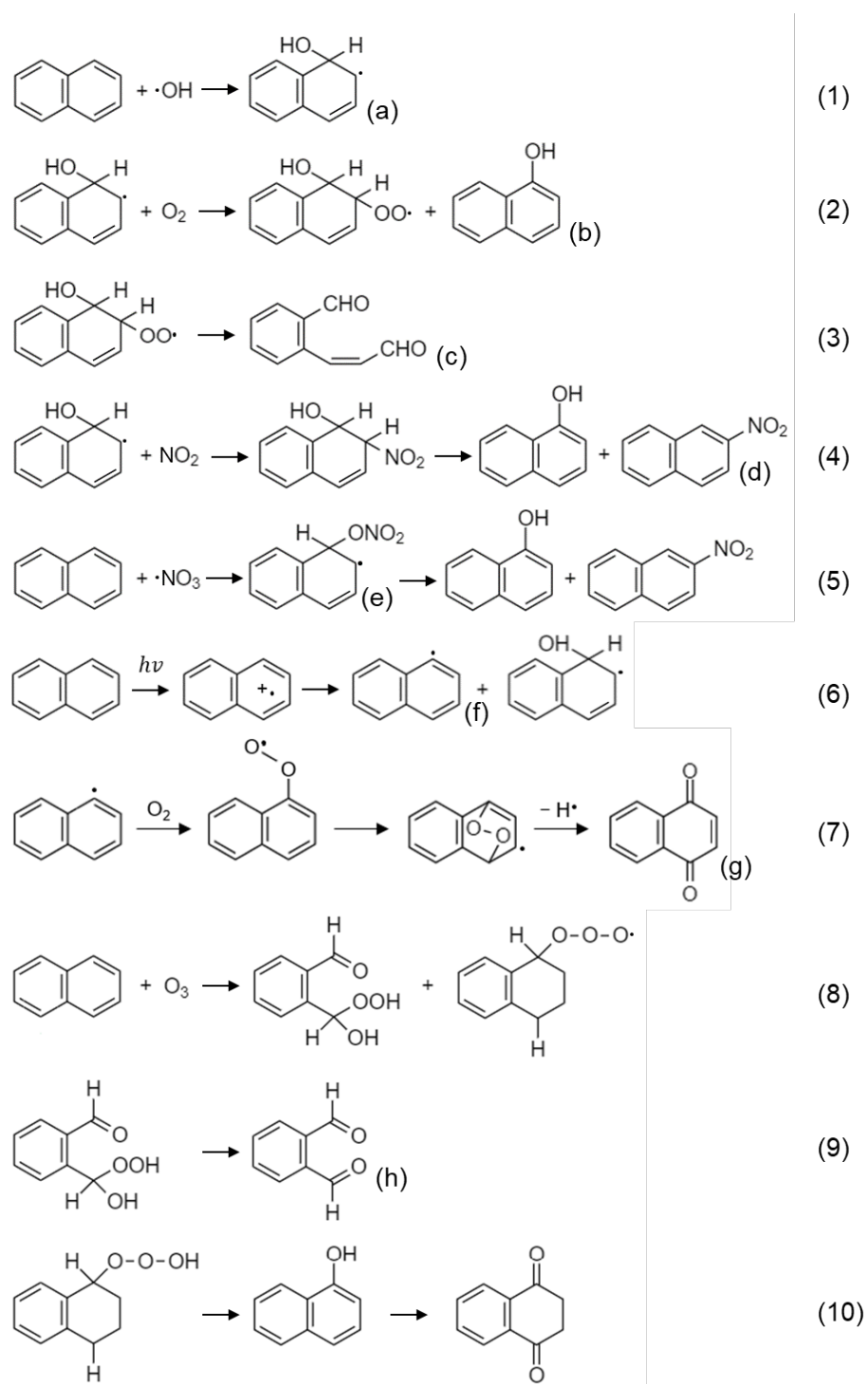
Fig. 3-1. Previously proposed reaction pathways of Nap. Reactions (1) and (2) were proposed by Bunce and Zhu (1995). Reactions (3) to (5) were proposed by Sasaki et al. (1997). Reaction (6) was proposed by Vialaton et al. (1999). Reactions (7) to (10) were proposed by Raja and Valsaraj (2005).

As regards other PAHs, quinones, hydroxylated and nitrated derivatives are the main products (Marquès et al., 2016, 2017). Most of these products have stronger polarity and chemical activity than their parent PAHs and act as important intermediates of SOA in the atmosphere (Ringuet et al., 2012; Zhang et al., 2011). More importantly, due to the direct-acting mutagenicity and the promotion of ROS production, oxygenated and nitrated PAHs can enhance the cytotoxicity and genotoxicity of atmospheric particles (Durant et al., 1996; Jariyasopit et al., 2014). Therefore, atmospheric chemical processes of PAHs can change atmospheric composition and influence its health effects.

Although the gas phase reaction is the main way to remove PAHs from the atmosphere, the heterogeneous reactions of PAHs may generate different products (Raja and Valsaraj, 2005; Zhang et al., 2011). The nature of atmospheric particles plays an essential role in the mechanism and rate of heterogeneous reactions of PAHs. For example, the reaction rate of PAHs on the nonpolar surface was higher than that on the polar surface (Bedjanian et al., 2010), and the nonpolar surface had a stronger affinity for O_3 (Ma et al., 2010); the increase of liquid water on the particle surface inhibited the formation of OH radicals (Luo et al., 2019), while some metal oxides and phenols could act as catalysts and photosensitizers for the reaction of PAHs, respectively (Wu et al., 2015; Zhu and Zhou, 2019). In addition, dark particle surfaces would absorb light and slow down the photodegradation of PAHs (Behymer and Hites, 1988).

On the surface of mineral particles, the conversion of PAHs could be promoted by active radicals, electron transfer, or Fenton-like reactions (Han et al., 2016; Shi et al., 2011; Zhao et al., 2019). However, many laboratory studies were limited to coating PAHs on the surface of mineral particles (Kameda et al., 2016; Marquès et al., 2016, 2017), ignoring the inherent deficiency of natural Kosa on PAHs and the collision between particle surfaces and PAH molecules. Moreover, a single mineral was mostly used as a surrogate to simulate the

reaction with little regard for the hygroscopicity of Kosa (Ma et al., 2010; Reyes et al., 2000; Zhao et al., 2019). These experiments underestimated the mineralogy of Kosa and the importance of surface water and amplified the role of a specific mineral.

Based on the defective experimental design of previous studies, this study adopted authentic Kosa particles and simulated the water layer on the particle surface to evaluate the substantial effect of Kosa on the chemical evolution of PAHs.

2 Materials and methods

2.1 Chemicals

Nap (99%), 1, 4-naphthoquinone (1, 4-NQ; 97%), HCl, H_2SO_4, and HNO_3 were provided by Wako Pure Chemical Industries, Ltd. (Osaka, Japan). All chemicals used in this study were of analytical reagent grade.

2.2 Batch reactivity experiments

The setup of the reactivity experiment is described in **Fig. 3-2**. Batch reactivity experiments were performed under various conditions, which were summarized in **Table 3-1**. A group of samples was performed in a batch experiment under the same conditions. In the experiment, 1.5 g of Kosa particles was placed in a 100 mL quartz conical flask, and 300 μL of Nap solution (30 mg/L) was spiked to the conical flask to make the particle surface wetted. The top of the conical flask was sealed with parafilm. A group of samples were then placed in a reaction chamber under light or dark conditions at 20°C. It should be indicated that there was a trace of solution in each sample to simulate the state of water-saturated particles, but there was no excess liquid flowing between the wetted particles.

38
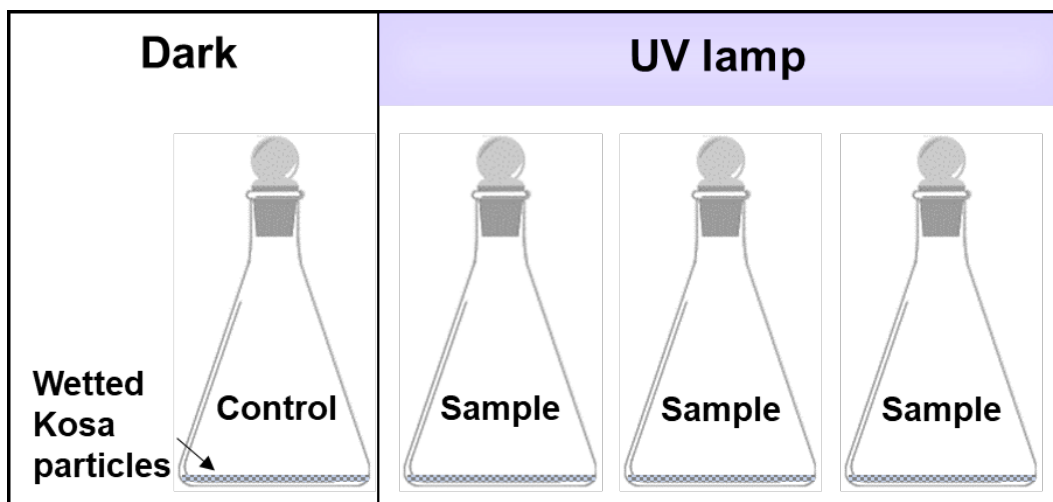
Fig. 3-2. Schematic diagram of the reactivity experiments. The control sample did not expose to UV radiation. The UV lamp can be adjusted by the switch at shortwave (254 nm) and longwave (365) UV radiations. The Kosa particles were wetted with the Nap solution.

Table 3-1. Conditions for batch reactivity experiments.

Conditions	Settings	Equipment / Material
Light / Dark	254 nm UV / 365 nm UV / Dark	UV lamp (UVGL-58, 6 W, Funakoshi Co., Ltd., Tokyo, Japan)
Acid / Acid-free	pH = 4.5 / pH = 7.5 ~ 8.8	With acid (H_2SO_4 / HNO_3 / HCl) / Without acid
Particle surface	Water-saturated / Water-free	Ultrapure water and methanol Trace amount of methanol to prevent the volatilization of Nap
Reaction time	0 ~ 6 h (interval: 0.5 h)	Take out at a predetermined time

After a predetermined time, a sample was taken out for treatment and analysis. First, 3.0 mL of methanol was added to the sample, and the conical flask was placed on a mixer to bring the methanol into full contact with Kosa particles. After standing for 5 min, the solution was centrifuged at 3500 rpm for 15 min to precipitate Kosa particles, and 20 μL of the supernatant was injected into the HPLC system for analysis.

2.3 Chemical analysis

The Nap and products were analyzed by the HPLC system following the methods described in Chapter 2. The recovery of 1, 4-NQ was 91%. The detection and quantification limits of 1, 4-NQ were 4.26 ng L^{-1} and 14.2 ng L^{-1}, respectively. The standard curve of 1, 4-NQ was linear, and the R^2 was 0.9998.

2.4 Product identification

During the HPLC analysis, each product was separated from the sample and collected to a volume of about 50 mL. The solution of the separated product was transferred to a separatory funnel with 50 mL of dichloromethane. Then, the separatory funnel was shaken up and down vigorously to make the solution fully contact. After standing for 10 min, the lower dichloromethane extract flowed into a concentration tube and was concentrated to 1 mL by a pressure blowing concentrator (MG-3100, Tokyo Rikakikai CO., LTD., Tokyo, Japan). The concentrate of each product was transferred to a vial for qualitative analysis.

The concentrate of each product was analyzed by gas chromatography-mass spectrometry (GC-MS) (Agilent 6890-5793, Agilent Technologies Inc., U.S.) with a DB-5MS capillary column (30 + 10 m × 0.25 i.d., 0.25 film thickness, Agilent Technologies Inc., U.S.). The injection was performed in splitless mode, helium was used as a carrier gas, and the flow rate was 1 mL min^{-1}. The temperature programs were set as follows: injector at

300°C; ion source at 150°C; quadrupole at 200°C; the column was time-programmed at 70°C for 1 min, then increased to 150°C at a rate of 10°C min⁻¹, held for 1 min, increased to 200°C at 20°C min⁻¹, held for 5 min. The analysis of products was performed in a scan mode at the mass-to-charge ratio (*m/z*) range of 50 to 200. The product was recognized firstly by comparing the mass spectra with the reference spectra in the NIST library. After that, the retention time of the product and the authentic compound in GC chromatograms were compared. If both the chromatogram and mass spectra agree with the authentic compound, the product can be determined.

2.5 Reaction kinetics

The kinetic profile, i.e. temporal variation, of Nap and the products was described uniformly by the relative change of the peak area to the initial peak area of Nap (A/A_0). The peak area of each compound was obtained by integrating the corresponding peak analyzed by the HPLC system.

The photodegradation of Nap under 254-nm UV radiation was estimated by the quasi-first-order kinetic model. Since two main products have been detected, the photodegradation of Nap was regarded as two parallel reactions, and its kinetics were estimated by **Eq. 3-1** and **Eq. 3-2**. The kinetics for the first 0.5 h of photodegradation was estimated to minimize the impact of the subsequent reactions of the products.

$$C_N = C_{N_0} \times e^{-(k_1+k_2)t} \tag{Eq. 3-1}$$

$$C_2 = \frac{k_2 \times C_{N_0}}{k_1+k_2} \times \left[1 - e^{-(k_1+k_2)t}\right] \tag{Eq. 3-2}$$

where C_N and C_2 are the molar concentration of Nap and product 2 (P 2) at 0.5 h, respectively, M; C_{N_0} is the initial molar concentration of Nap, M; k_1 and k_2 are the rate constant of the conversion of Nap to product 1 (P 1) and P 2, respectively, min⁻¹.

3 Results

3.1 Reaction in the aqueous solution

Fig. 3-3 presents the HPLC chromatograms of the blank samples after 0.5 h of reaction under different UV irradiation and dark conditions. Under dark conditions (black curve) and 365-nm UV irradiation (red curve), only the solvent and Nap peaks appeared in the chromatograms. However, two small peaks other than the solvent and Nap peaks were observed in the blank exposed to 254-nm UV radiation (green curve), which were considered as the primary photodegraded products of Nap. The retention time of the products P 1 and P 2 was 6.97 min and 8.97 min, respectively. In addition, P 1 and P 2 were detected in the methanol solution of Nap under 254-nm UV irradiation (yellow curve), and no other products were observed. This finding indicates that Nap underwent a consistent degradation in the aqueous and methanol solutions under 254-nm UV irradiation. Moreover, the signal intensity of P 1 and P 2 detected in the methanol solution was lower than that in the aqueous solution under the same experimental conditions. Therefore, a small amount of methanol in the aqueous solution had negligible effect on the photodegradation of Nap.

Fig. 3-4 shows the temporal variation of Nap and the products in the blank under different UV irradiation and dark conditions. As shown in **Fig. 3-4a**, the content of Nap in the blank decreased with reaction time under both light and dark conditions. The downward trend of Nap was consistent under dark conditions and 365-nm UV irradiation, and the A/A_0 of Nap after 6 h of reaction was 89.6% and 84.3%, respectively. The reduction in Nap was driven by volatilization under dark conditions and 365-nm UV irradiation due to the absence of products, while in the blank exposed to 254-nm UV radiation, it was attributed to volatilization and photodegradation. In addition, the A/A_0 of the products showed an upward trend with reaction time (**Fig. 3-4b**), and the increase in P 1 was greater than P 2.
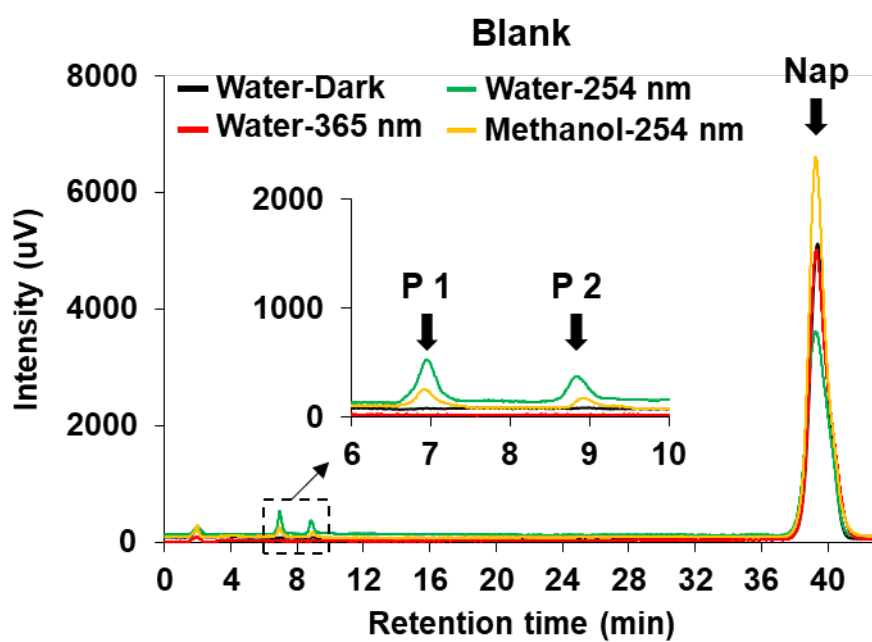
Fig. 3-3. Chromatograms of the blank samples under different conditions at the first 0.5 h of reaction. P1 is product 1. P 2 is product 2.
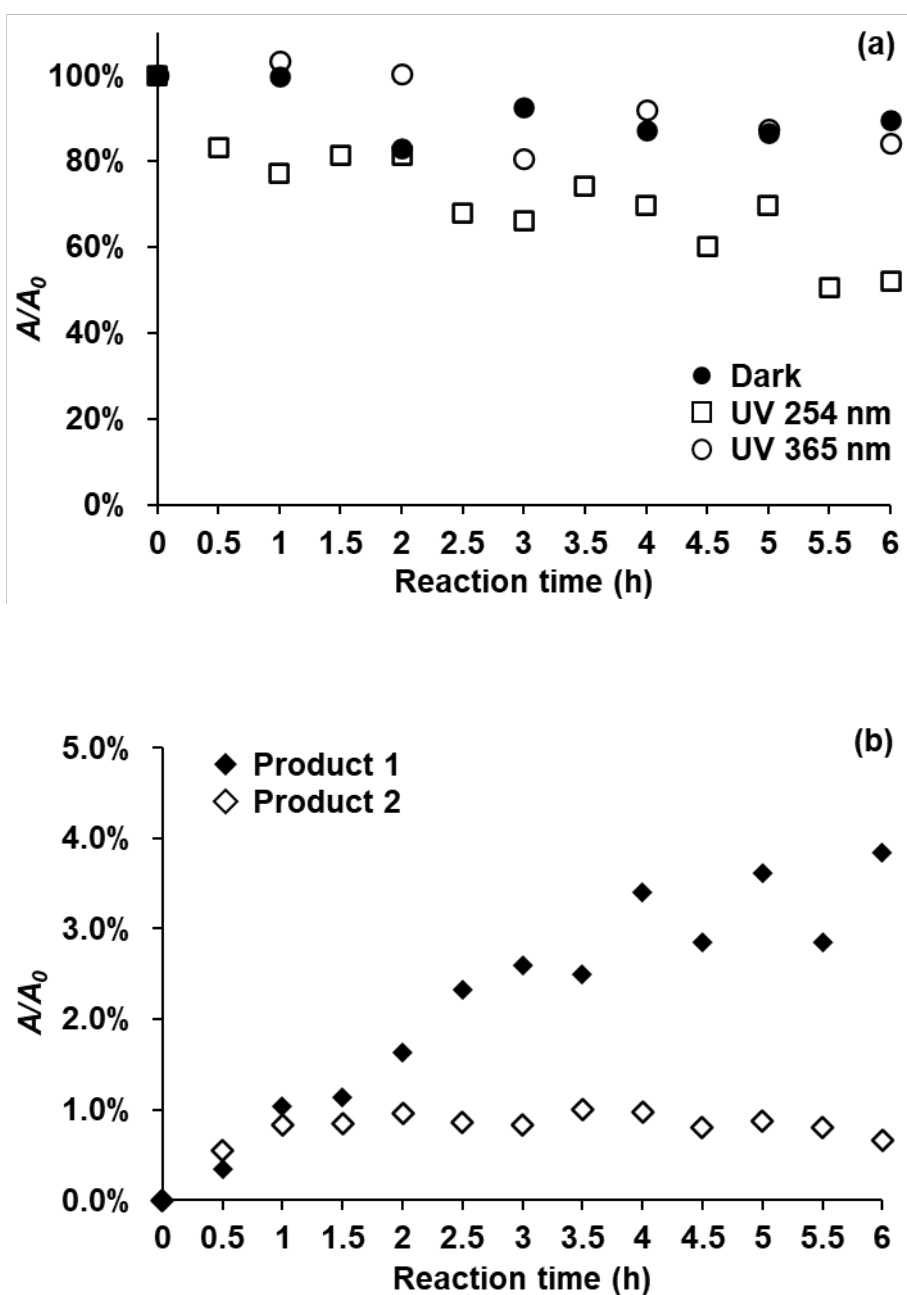
Fig. 3-4. Temporal variation in (a) Nap under different UV irradiation and dark conditions, (b) products formed under 254-nm UV irradiation in the blank samples. *A* is the chromatogram peak area of Nap and the products. A_0 is the initial chromatogram peak area of Nap.

3.2 Reaction in the saturated water layer of Kosa particles

Fig. 3-5 shows the HPLC chromatograms of samples containing Kosa 1 particles under different conditions. The chromatographic peaks detected in the samples containing the other three Kosa particles were consistent with those of Kosa 1. In the samples under dark conditions (black curve) and 365-nm UV irradiation (red curve), only the solvent and Nap peaks were detected. In the chromatogram of the sample exposed to 254-nm UV radiation (green curve), the peaks of solvent, P 1, P 2, and Nap appeared, and there were no peaks of other possible products. Moreover, the peaks of solvent, P 1, P 2, and Nap were detected in the anhydrous sample exposed to 254-nm UV radiation (yellow curve). This was due to the residual methanol on the anhydrous surface of Kosa 1 particles to prevent Nap from rapid volatilization. These observations indicate that Kosa particles would not induce the degradation of Nap on both the water-saturated and anhydrous surface. In addition, the intensity of UV radiation and the presence of water could affect the photodegradation of Nap.

The chromatograms of the samples exposed to 254-nm UV radiation under acid conditions are shown in **Fig. 3-5**. The consistent peaks appeared in the chromatograms of samples under acidic and acid-free conditions, which indicates that the acidification of the surface of Kosa particles would not change the photodegradation pathway of Nap.

Fig. 3-6 and **Fig. 3-7** show the temporal variation of Nap in the saturated water layer of the four Kosa particles under different conditions. Under dark conditions and 365-nm UV irradiation (**Fig. 3-6**), the temporal variation of Nap in the saturated water layer was identical with that in the aqueous solution (**Fig. 3-4a**), which was driven by the volatilization of Nap. Under 254-nm UV irradiation, the Nap in the saturated water layer of Kosa particles showed a consistent downward trend under acid and acid-free conditions (**Fig. 3-7**). In addition, the decrease in Nap in the blank exposed to 254-nm UV radiation (**Fig. 3-4a**) was greater than that in the saturated water layer of the four Kosa particles under the same conditions.
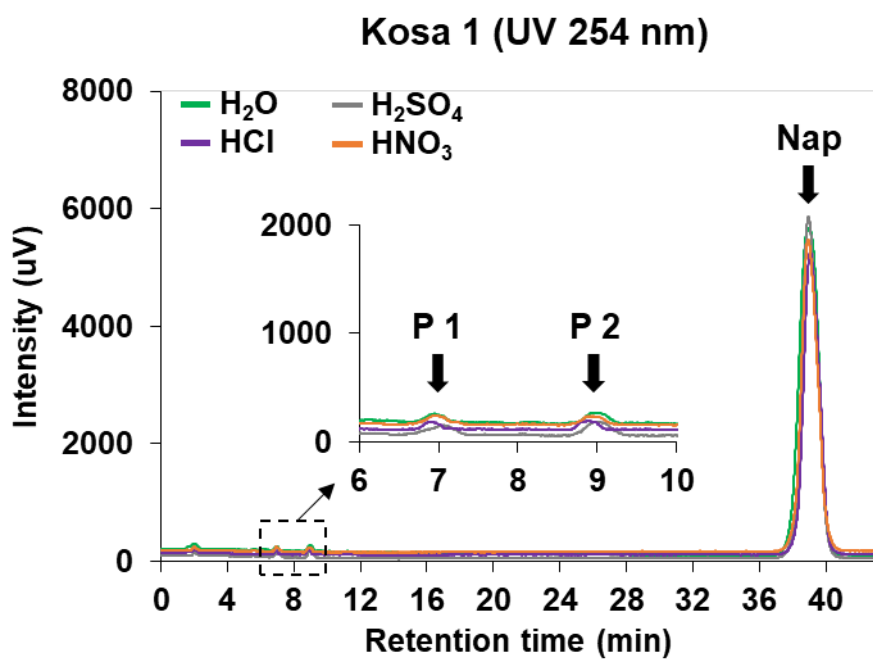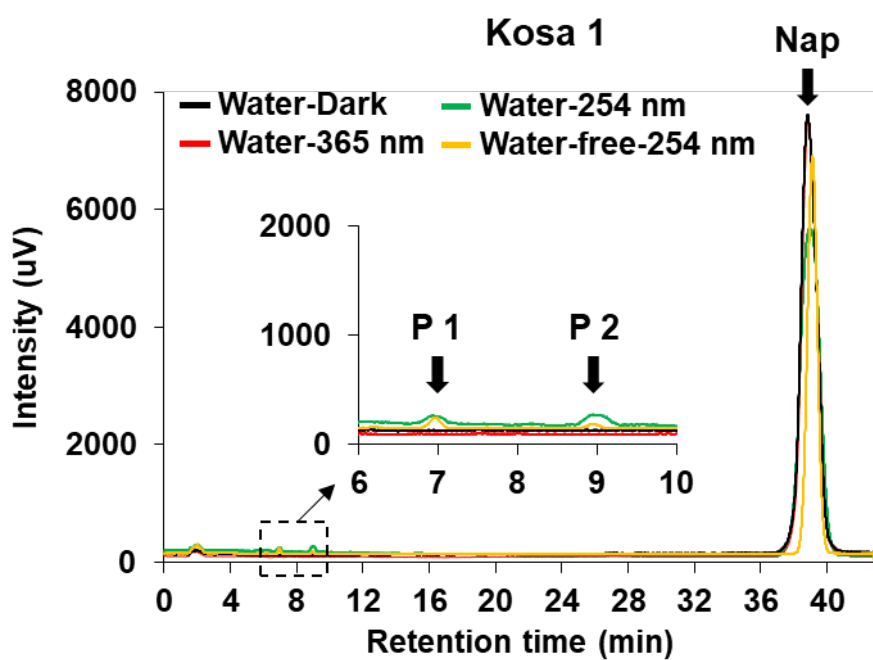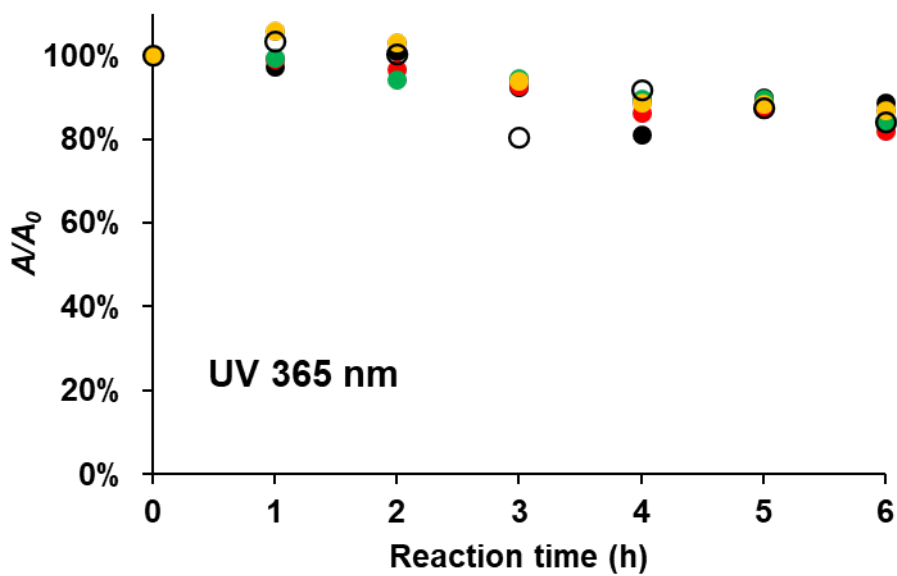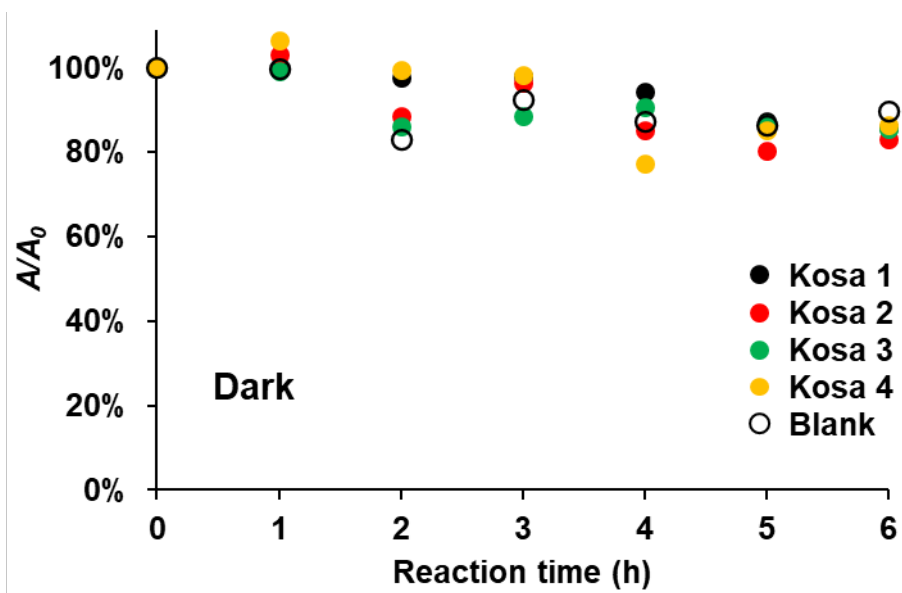
Fig. 3-5. Chromatograms of the samples containing Kosa 1 particles under different conditions.

Fig. 3-6. Temporal variation in Nap in different samples under dark conditions and 365-nm UV irradiation.
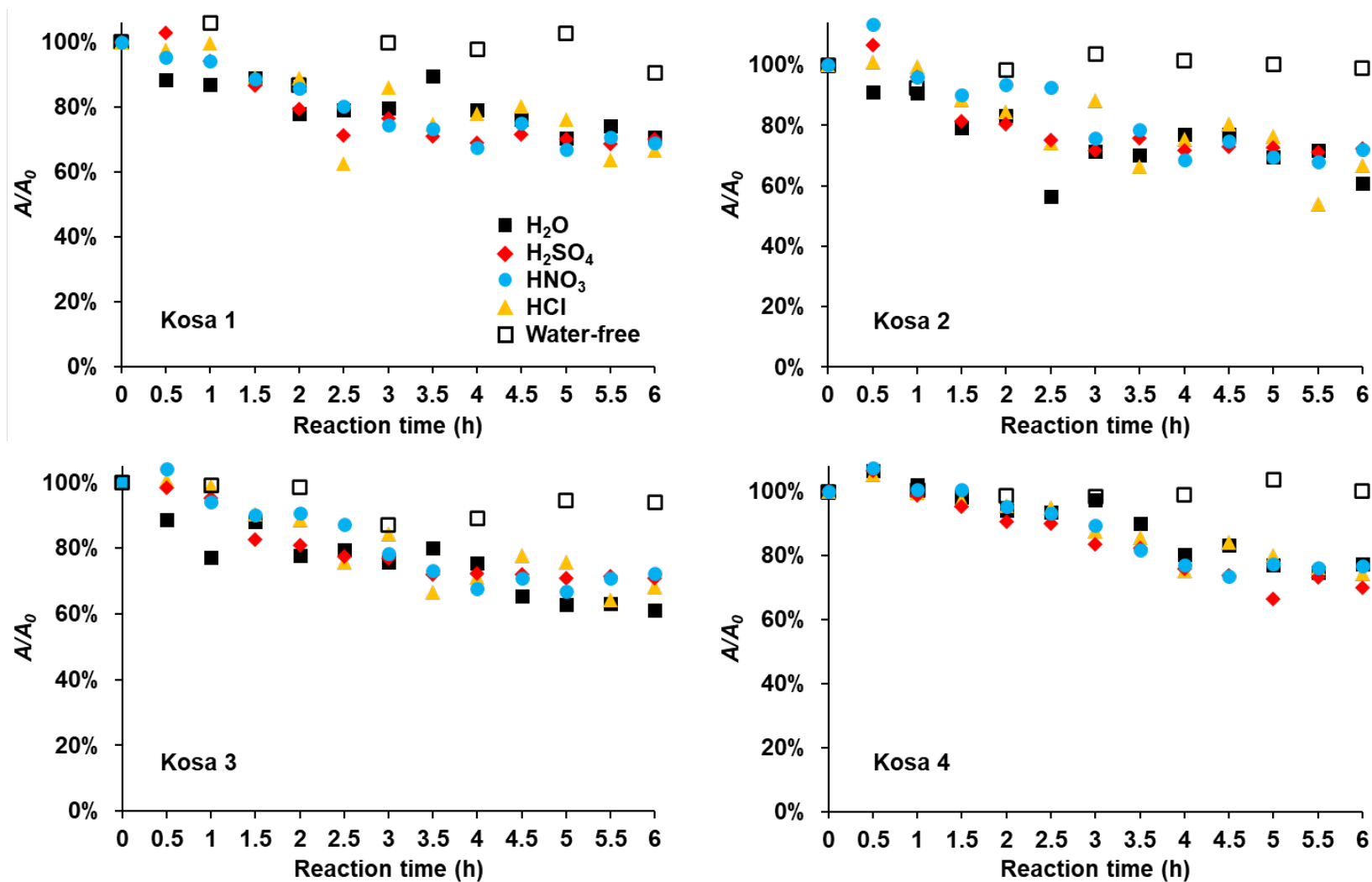
Fig. 3-7. Temporal variation in Nap in different samples under 254-nm UV irradiation.

The temporal variation of P 1 and P 2 in the saturated water layer of the four Kosa particles is presented in **Fig. 3-8** and **Fig. 3-9**, respectively. By comparison with acid-free conditions, acid conditions had little effect on the upward trend of P 1 and P 2. Moreover, the production efficiency of P 1 and P 2 in the saturated water layer of the four Kosa particles was lower than that in the blank (**Fig. 3-4b**) under the same conditions. These observations indicate that Kosa particles did not accelerate the photodegradation of Nap but caused a slower photodegradation process. This might be due to the scattering and absorption of UV radiation by the Kosa particles slowed down the photodegradation of Nap (Jeong and Nousiainen, 2014). Compared with the other three Kosa particles, the reduction in Nap and the increases in P 1 and P 2 were moderated in the saturated water layer of the Kosa 4 particles. This might be because Kosa 4 particles were finer and had a higher number density than the other three Kosa particles at the same mass, causing a more efficient extinction of light.

In addition, under 254-nm UV irradiation, the photodegradation of Nap on the anhydrous surface of Kosa particles was slower than in the saturated water layer (**Fig. 3-7**, **Fig. 3-8**, and **Fig. 3-9**). This finding emphasizes the important role of surface water in the photodegradation rate of Nap.
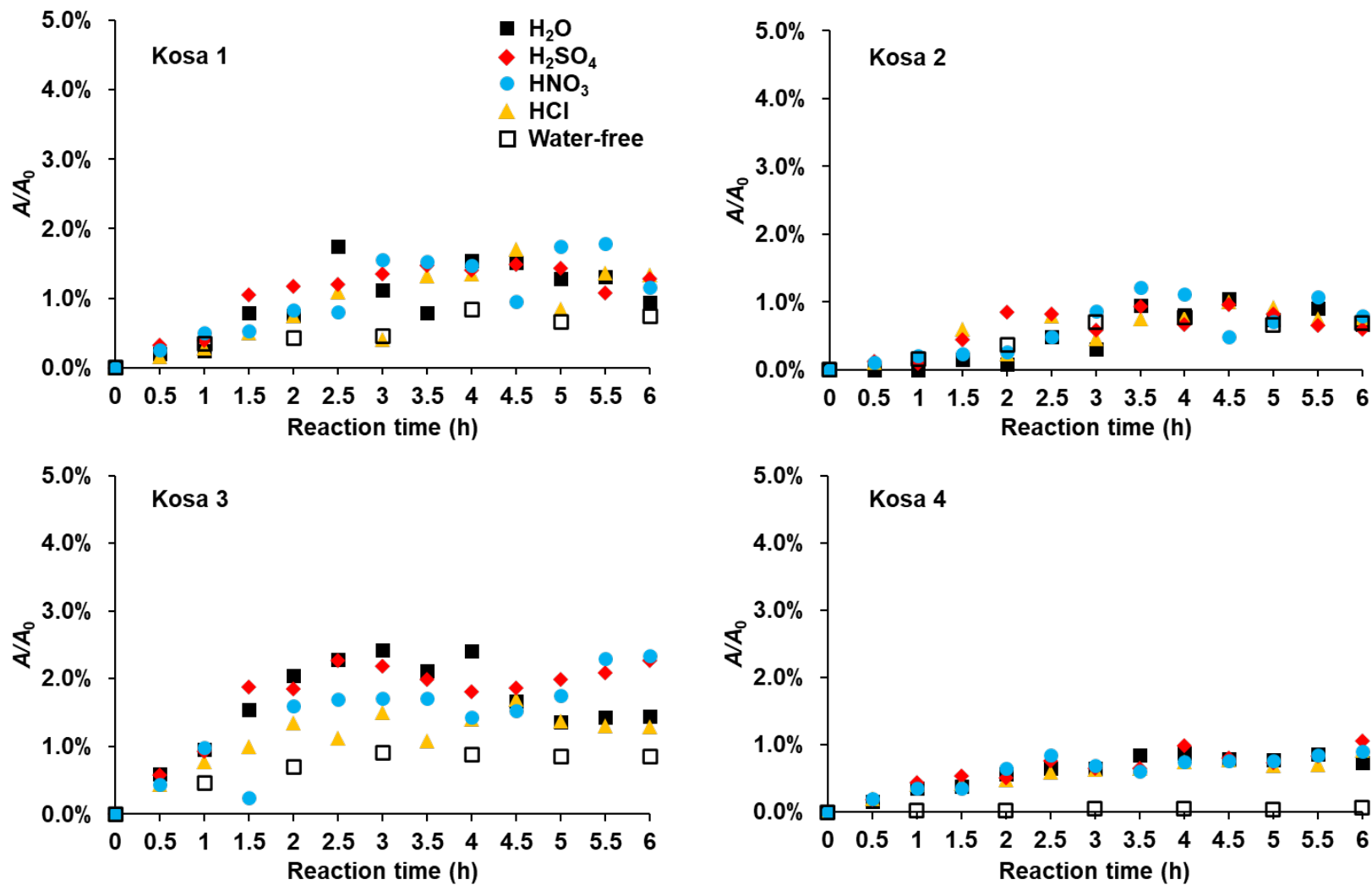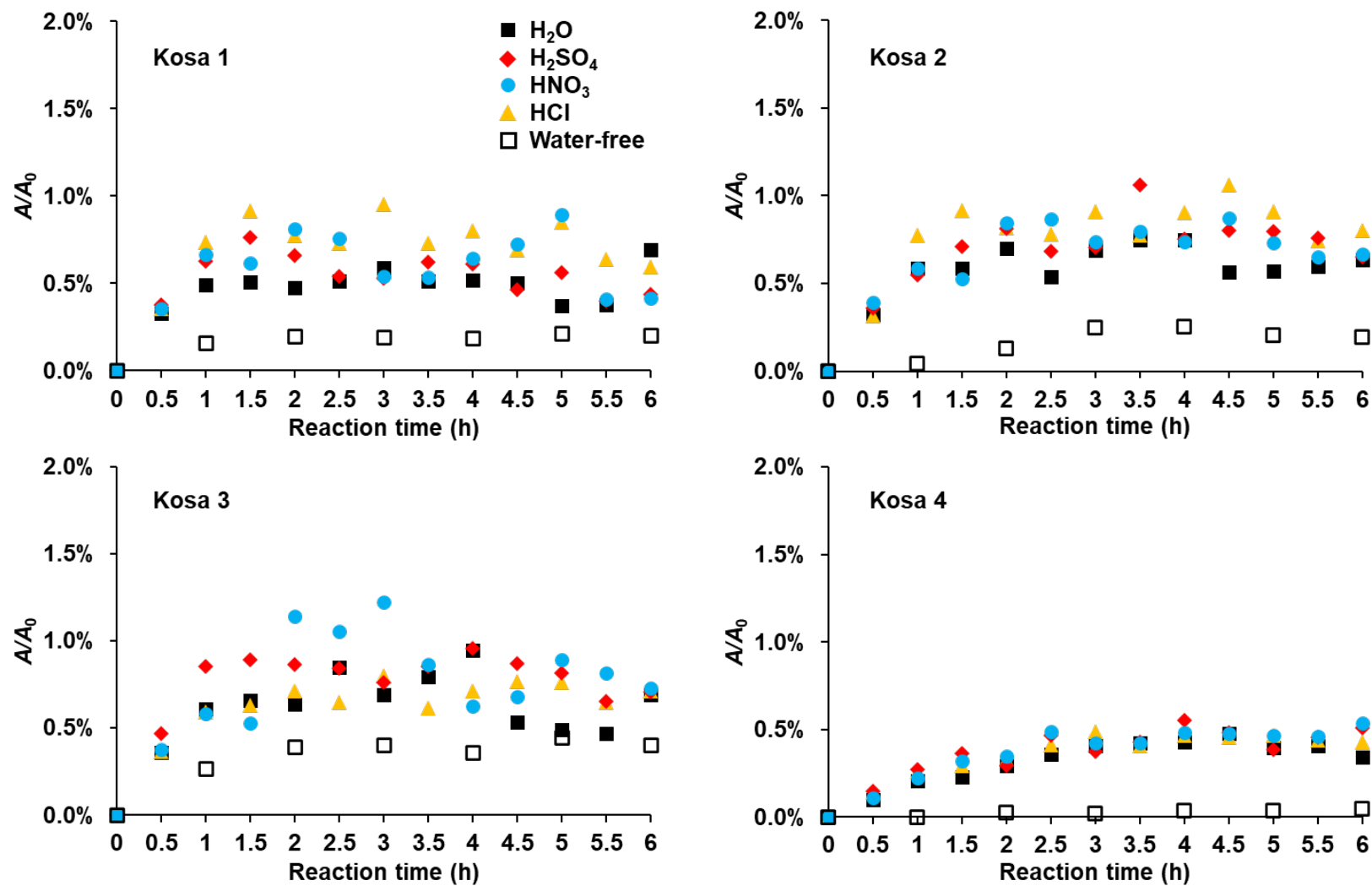
Fig. 3-8. Temporal variation in P1 in different samples under 254-nm UV irradiation.

Fig. 3-9. Temporal variation in P2 in different samples under 254-nm UV irradiation.

3.3 Product identification

Fig. 3-10 is the mass spectrum of P 1, showing obvious base peak (*m/z* 131) and three fragment ion peaks (*m/z* 105, 77, and 51), and the molecular ion peak (*m/z* 160) that was easily overlooked. These structural characteristics were consistent with the product generated in the photodegradation of Nap in water and the gas phase reaction between Nap and OH radicals (Sasaki et al., 1997; Vialaton et al., 1999), which was recognized as 2-formylcinnamaldehyde (2-FCA) by nuclear magnetic resonance (NMR) (Sasaki et al., 1997). Since the authentic compound of 2-FCA is unavailable at present, P 1 has not been further qualitatively analyzed in this study. Nevertheless, based on the consistent results of this study and previous studies, P 1 was considered to be 2-FCA.

Fig. 3-11 shows the GC chromatograms and mass spectrums of P 2 and 1, 4-NQ. Due to the high consistency between P 2 and 1, 4-NQ in the retention time of the chromatographic peak (10.9 min) and the structural characteristics (*m/z* 158, 130, 104, 102, 76, and 50) detected by MS, P 2 was identified as 1, 4-NQ. The results of previous studies indicated that 1, 4-NQ was a major photodegraded product of Nap in water (Tuhkanen and Beltrán, 1995).
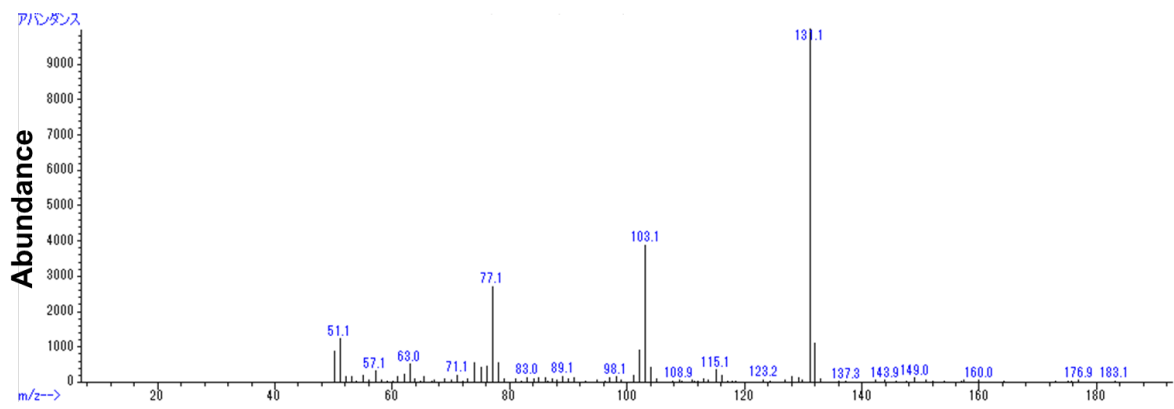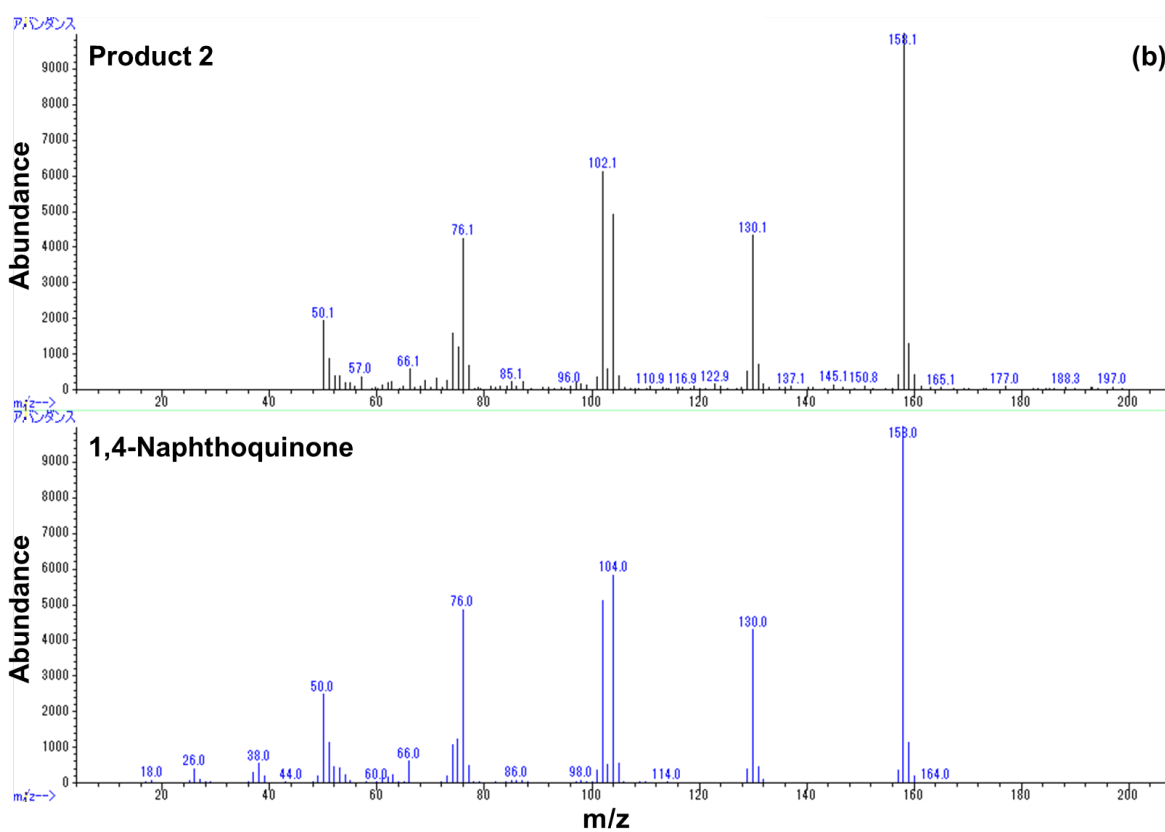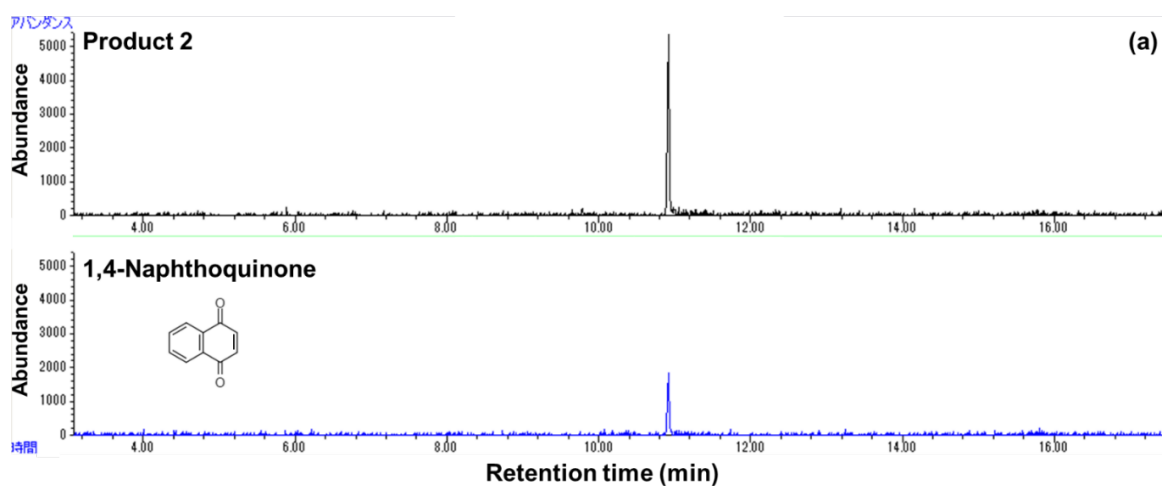
Fig. 3-10. Mass spectra of P 1.

Fig. 3-11. Comparison of (a) GC chromatogram and (b) mass spectra between P 2 and 1, 4-naphthoquinone.

3.4 Photodegradation kinetics

Fig. 3-12 presents the photodegradation kinetics of Nap in the aqueous and methanol solutions exposed to 254-nm UV radiation, which were according with the linear form of quasi first order equation (R^2 = 0.784 and 0.992, respectively). The photodegradation rate constants of Nap in the aqueous and methanol solutions were estimated as 8.55×10^{-4} min^{-1} (k_a) and 1.44×10^{-4} min^{-1} (k_m), respectively. Under 254-nm UV irradiation, Nap in the aqueous solution underwent photodegradation and volatilization simultaneously, whereas Nap in the methanol solution was photodegraded more slowly and volatilized minimally. Therefore, the net photodegradation rate constant of Nap in the aqueous solution was between k_m and k_a. Similarly, under 254-nm UV irradiation, the net formation rate constant of 1, 4-NQ in the aqueous solution was between 4.85×10^{-6} min^{-1} (in the methanol solution) and 2.01×10^{-5} min^{-1} (in the aqueous solution). Moreover, the net formation rate constant of 2-FCA in the aqueous solution should be between 1.40×10^{-4} min^{-1} (in the methanol solution) and 8.35×10^{-4} min^{-1} (in the aqueous solution) in the absence of other parallel reactions. In the saturated water layer of Kosa particles, the rate constants of Nap photodegradation and product formation under 254-nm UV irradiation were expected to be smaller than in the aqueous solution.
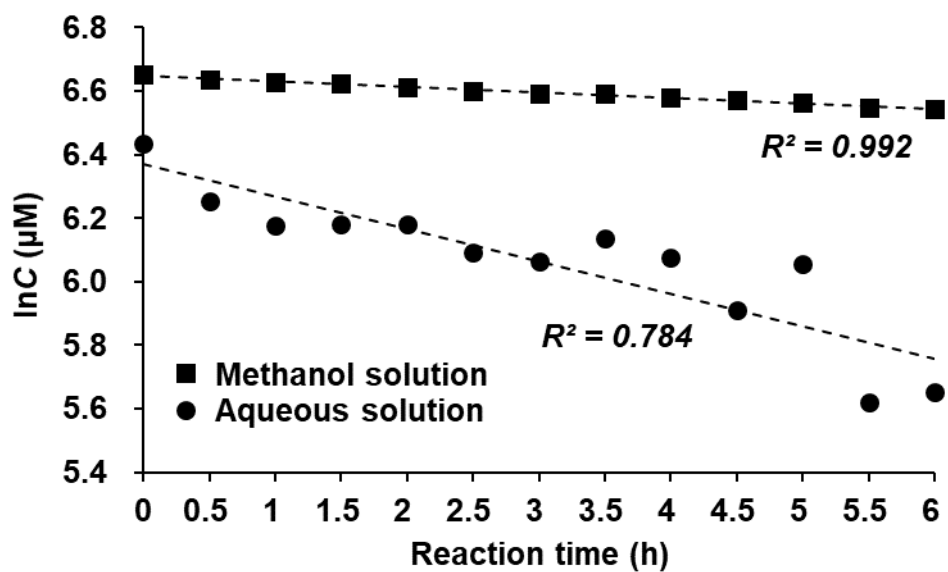
Fig. 3-12. Photodegradation kinetics of Nap in the aqueous and methanol solutions under 254-nm UV irradiation. C is the molar concentration of Nap, μM.

4 Discussion

Fig. 3-13 is the scheme of the conversion of Nap to 2-FCA and 1, 4-NQ in the aqueous phase under 254-nm UV irradiation. These mechanisms were proposed based on the experimental results of this study and the conclusions of previous studies (Bunce and Zhu, 1995; Sasaki et al., 1997; Vialaton et al., 1999). Since there were no active radicals (such as OH radicals) and relevant precursors (such as NO_2 and O_3) provided in the present experimental system (Shiraiwa et al., 2009), the aqueous photodegradation of Nap was initiated by photoionization (Vialaton et al., 1999). After Nap donates electrons, the free radical cations of Nap are produced and then converted to active intermediates (free radicals R 1 and R 2) via deprotonation or the addition of H_2O (**Fig. 3-13**). With the participation of O_2, R 1 and R 2 undergo a series of reactions to produce 1, 4-NQ and 2-FCA. In addition, previous studies have indicated that 3- and 4-ring PAHs can generate quinones by direct photolysis as that of Nap (Jariyasopit et al., 2014).

2-FCA and 1, 4-NQ are cytotoxic and genotoxic, leading to higher health risks in humans than Nap (Wilson et al., 1996); additionally, they can continue to degrade after being generated in the atmosphere and are important contributors to SOA (Bunce and Zhu, 1995; Vialaton et al., 1999). In this study, a slight secondary conversion of 2-FCA and 1, 4-NQ were observed, which showed a milder upward trend of relative abundance in the later stage of the reaction (**Fig. 3-4**, **Fig. 3-7**, and **Fig. 3-8**). However, the signal intensity of the secondary products detected by HPLC was weak and difficult to be separated and identified.
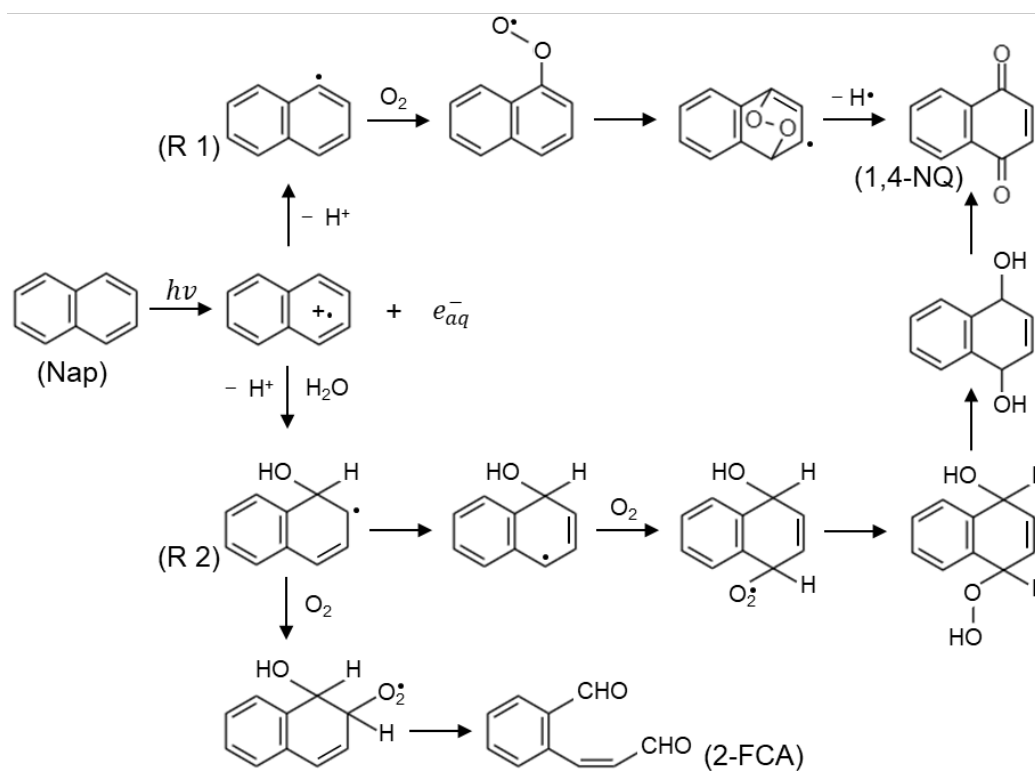
Fig. 3-13. Proposed photodegradation scheme of Nap in the aqueous solution under 254-nm UV irradiation based on previous reports (Bunce and Zhu, 1995; Sasaki et al., 1997; Vialaton et al., 1999). R represents the radial immediate of Nap.

Based on the results of previous research, under 375-nm UV irradiation, the oxidation rate constant of Nap initiated by OH radicals in the gas phase was 0.035 min^{-1} (Bunce et al., 1997), which was about two orders of magnitude higher than the photodegradation rate constant of Nap in the aqueous phase under 254-nm UV irradiation (between 1.44×10^{-4} min^{-1} and 8.55×10^{-4} min^{-1}). In addition, in the gas phase reaction between Nap and OH radicals, the formation rate constant of 2-FCA was 2.28×10^{-3} s^{-1} (Nishino et al., 2009), which was much higher than the results of this study (between 1.40×10^{-4} min^{-1} and 8.35×10^{-4} min^{-1}). On the other hand, most UVA (wavelength ranges in 320-400 nm) and a small amount of UVB (wavelength ranges in 280-320 nm) can penetrate the atmosphere to reach the ground, while highly intensive UVC (wavelength ranges in 100-280 nm) is blocked by the ozone layer (Marquès et al., 2017). Therefore, from the perspective of reaction rates and conditions, the aqueous photodegradation is unlikely to be a major reaction pathway of Nap in the atmosphere. Moreover, the photodegradation of Nap in the water layer of Kosa particles is more disadvantaged in the atmosphere.

In addition, the intensity of UV radiation is higher in countries or regions near the equator and at high altitudes. Meanwhile, there are significant sources of PAHs and water vapor in these areas (Williamson et al., 2019), such as Rwanda in Central Africa (Kalisa et al., 2018). In the liquid water of aerosols or atmospheric particles, the aqueous photodegradation might be an important reaction path of PAHs in these areas, which can change the local atmospheric composition and the toxicity of atmospheric particles.

In conclusion, the photodegradation of Nap in the aqueous phase could be initiated by photoionization in the absence of active oxidants, and the primary products were 2-FCA and 1, 4-NQ. Kosa particles did not induce or promote the photodegradation of Nap in the aqueous and anhydrous conditions, whereas the presence of water and the intensity of UV

radiation were important factors affecting the photodegradation process. Moreover, the extinction of light by the Kosa particles could slow down the photodegradation of Nap and the formation of products in the saturated water layer. In addition, the rate constants of Nap photodegradation and product formation in the aqueous phase were far below those of the gas phase reaction of Nap with OH radicals. Therefore, the aqueous photodegradation is not a major pathway for the atmospheric conversion of Nap, and Kosa particles have no substantial effect on this process.

Summary

In this study, Kosa samples were collected from typical deserts in East Asia, including the Gobi Desert, Taklimakan Desert, Horqin Sandy Land, and Loess Plateau. The physical properties and the composition of metallic elements and water-soluble inorganic ions of the four Kosa samples were measured. Then, the adsorption capacity of different Kosa particles to Nap was evaluated by conducting batch adsorption experiments. Based on the hygroscopicity of the Kosa particles, the reaction of Nap in the aqueous solution and saturated water layer of Kosa particles was investigated under various conditions to clarify the effect of Kosa on the conversion of Nap. The main results are as follows.

(1) The size, specific surface area and total pore volume of the four types of Kosa particles were measured, showing obvious regional differences. Compared with those from the Gobi Desert, Taklimakan Desert, and Horqin Sandy Land, Kosa particles collected from the Loess Plateau had the finest size, and the highest specific surface area and total pore volume. The pore size of the four Kosa particles was comparable to the mesoporous materials. In addition, the four Kosa particles were characterized by high-level crustal elements and low-level transition metals, but the element contents differed greatly. The composition of water-soluble inorganic ions of the four Kosa particles also varied with geographical origin. Kosa particles originating in the Gobi Desert and Taklimakan Desert were richer in Na^+ and Cl^-, while those originating in the Horqin Sandy Land and Loess Plateau were more abundant in Ca^{2+}, SO_4^{2-}, and NO_3^-. Nevertheless, these ions can promote the hygroscopic behavior of Kosa particles.

(2) Kosa particles collected from the Loess Plateau were found to have weak physical adsorption of Nap, which was well represented by the Langmuir isotherm model. However, Kosa particles from the other three deserts had no obvious adsorption of Nap, which was

attributed to their limited specific surface area and total pore volume. Compared with microporous minerals and particles with the nonpolar surface, Kosa particles were disadvantaged in the adsorption capacity and affinity of Nap and more hydrophobic PAHs. In addition, the acidification of the surface of Kosa particles could inhibit the adsorption of Nap. Therefore, Kosa particles are not regarded as a good carrier for PAHs in the atmosphere.

(3) Under dark conditions and 365-nm UV irradiation, no chemical reactions occurred in the aqueous solution, and the reduction in Nap was driven by volatilization. When exposed to 254-nm UV radiation, the Nap underwent degradation initiated by photoionization and the primary products were 2-FCA and 1, 4-NQ. The photodegradation rate constant of Nap in the aqueous phase was between 1.44×10^{-4} min^{-1} and 8.55×10^{-4} min^{-1}, which was far below the rate constant of gas phase reaction between Nap and OH radicals. Unexpectedly, Nap in the saturated water layer of Kosa particles experienced the same photodegradation as in the aqueous solution. Moreover, Kosa particles did not induce or promote the conversion of Nap but slowed down the photodegradation of Nap via the scattering and absorption of UV radiation. In addition, the water content and UV intensity were important factors affecting the aqueous photodegradation of Nap.

The above results indicate that there are substantially no physical and chemical interactions between Kosa particles and PAHs. This finding suggests that Kosa from the Asian continent are not effective carriers and catalysts for PAHs in the atmosphere, which is contrary to the preconceptions.

References

Ames, B.N., McCann, J., and Yamasaki, E. Method for detecting carcinogens and mutagens with the salmonella/mammalian-microsome mutagenicity test. *Muta. Res.,* 31, 347–364 (1975)

Araki, Y., Tang, N., Ohno, M., Kameda, T., Toriba, A. and Hayakawa, K. Analysis of atmospheric polycyclic aromatic hydrocarbons and nitropolycyclic aromatic hydrocarbons in gas/particle phases separately collected by a high-volume air sampler equipped with a column packed with XAD-4 resin. *J. Health Sci.,* 55 (1), 77–85 (2009)

Arey, J., Zielinska, B., Atkinson, R., Winer, A.M., Ramdahl, T. and Pitts, J.N. The formation of nitro-PAH from the gas-phase reactions of fluoranthene and pyrene with the OH radical in the presence of NOx. *Atmos. Environ.,* 20, 2339–2345 (1986)

Bagan, H., Takeuchi, W., Kinoshita, T., Bao, Y. and Yamagata, Y. Land cover classification and change analysis in the Horqin Sandy Land from 1975 to 2007. *IEEE J-STARS,* 3(2), 168–177 (2010)

Baxter, R.J. and Hu, P. Insight into why the Langmuir–Hinshelwood mechanism is generally preferred. *J. Chem. Phys.,* 116, 4379 (2002)

Bedjanian, Y., Nguyen, M.L. and Bras, G.L. Kinetics of the reactions of soot surface-bound polycyclic aromatic hydrocarbons with the OH radicals. *Atmos. Environ.,* 44, 1754–1760 (2010)

Behymer, T.D. and Hites, R.A. Photolysis of polycyclic aromatic hydrocarbons adsorbed on fly ash. *Environ. Sci. Technol.,* 22 (11), 1311–1319 (1988)

Bollinger, C., McCallister, M., Clark, R., Rhoades, R., Maguire, M., Savage, R., Jiao, Y., Ramesh, A. and Hood, D. Polycyclic aromatic hydrocarbons: implications for developmental, molecular, and behavioral neurotoxicity. Polycyclic Aromatic

Hydrocarbons Handbook of Toxicology of Chemical Warfare Agents (Second Edition), 249–265 (2015)

BP p.l.c. BP Statistical Review of World Energy 2019 https://www.bp.com/en/global/corporate/energy-economics/statistical-review-of-world-energy.html (2019)

Brody, J.G., Moysich, K.B., Humblet, O., Attfield, K.R., Beehler, G.P. and Rudel, R.A. Environmental pollutants and breast cancer. *Cancer,* 109, 2667–2711 (2007)

Bunce, N.J. and Zhu, J. Products from photochemical reactions of naphthalene in air. *Polycycl. Aromat. Comp.,* 5(1–4), 123–130 (1995)

Bunce, N.J., Liu, L., Zhu, J. and Lane, D.A. Reaction of Nap and its derivatives with hydroxyl radicals in the gas phase. *Environ. Sci. Technol.,* 31(8), 2252–2259 (1997)

Carroll, D. Rock Weathering: Monographs in Geoscience, first Ed. in 1970. Springer Science & Business Media, US (2012)

Chang, C.-F., Chang, C.-Y., Chen, K.-H., Tsai, W.-T., Shie, J.-L. and Chen, Y.-H. Adsorption of Nap on zeolite from aqueous solution. *J. Colloid Interface Sci.,* 277(1), 29-34 (2004)

Chen, L., Peng, C., Nenes, A., Gu, W., Fu, H., Jian, X., Zhang, H., Zhang, G., Zhu, J., Wang, X., and Tang, M. On mineral dust aerosol hygroscopicity. *Atmos. Chem. Phys. Discuss.,* https://doi.org/10.5194/acp-2020-442 (2020)

Choi, S.-D., Ghim, Y.S., Lee, J.Y., Kim, J.Y. and Kim, Y.P. Factors affecting the level and pattern of polycyclic aromatic hydrocarbons (PAHs) at Gosan, Korea during a dust period. *J. Hazard. Mater.,* 227–228, 79–87 (2012)

Cochran, R.E., Kubátová, A. and Kozliak, E.I. An approach to the estimation of adsorption enthalpies of polycyclic aromatic hydrocarbons on particle surfaces. *J. Phys. Chem. A,* 120(30), 6029–6038 (2016)

Cwiertny, D.M., Young, M.A. and Grassian, V.H. Chemistry and photochemistry of mineral

dust aerosol. *Annu. Rev. Phys. Chem.,* 59, 27–51 (2008)

Dang, J., Shi, X.L., Zhang, Q.Z., Hu, J.T., Chen, J.M. and Wang, W.X. Mechanistic and kinetic studies on the OH-initiated atmospheric oxidation of fluoranthene. *Sci. Total Environ.,* 490, 639–646 (2014)

Derbyshire, E., Meng, XM. and Kemp, A.B. Provenance, transport and characteristics of modern aeolian dust in western Gansu Province, China, and interpretation of the Quaternary loess record. *J. Arid Environ.,* 39, 497–516 (1998)

Dong, Z.S., Su, F.C., Zhang, Z.Y. and Wang, S.B. Observation of chemical components of $PM_{2.5}$ and secondary inorganic aerosol formation during haze and sandy haze days in Zhengzhou, China. *J. Environ. Sci.,* 88, 316–325 (2019)

Durant, J.L., Busby Jr, W.F., Lafleur, A.L., Penman, B.W. and Crespi, C.L. Human cell mutagenicity of oxygenated, nitrated and unsubstituted polycyclic aromatic hydrocarbons associated with urban aerosols. *Mutat. Res. Genet. Toxicol.,* 371, 123–157 (1996)

El zein, A., Dunmore, R.E., Ward, M.W., Hamilton, J.F., and Lewis, A.C. Variability of polycyclic aromatic hydrocarbons and their oxidative derivatives in wintertime Beijing, China. *Atmos. Chem. Phys.,* 19, 8741–8758 (2019)

Fairlie, T.D., Jacob, D.J., Dibb, J.E., Alexander, B., Avery, M.A., van Donkelaar, A. and Zhang, L. Impact of mineral dust on nitrate, sulfate, and ozone in transpacific Asian pollution plumes. *Atmos. Chem. Phys.,* 10, 3999–4012 (2018)

Fang, G.-C., Wu, Y.-S., Chen, J.-C., Fu, P.P.-C., Chang, C.-N., Ho, T.-T. and Chen, M.-H. Characteristic study of polycyclic aromatic hydrocarbons for fine and coarse particulates at Pastureland near industrial park sampling site of central Taiwan. *Chemosphere,* 60, 427–433 (2005)

Gnanaprakasam, M, Sandhiya, L. and Senthilkumar, K. A theoretical investigation on the

mechanism and kinetics of the gas-phase reaction of Nap with OH radical. *Theor. Chem. Acc.,* 136, 131 (2017)

Guo, Z.G., Sheng, L.F., Feng, J.L., and Fang, M. Seasonal variation of solvent extractable organic compounds in the aerosols in Qingdao, China. *Atmos. Environ.,* 37, 1825–1834 (2003)

Han, C., Yang, W.J., Yang, H. and Xue, X.X. Influences of O_2 and O_3 on the heterogeneous photochemical reaction of NO_2 with humic acids. *Atmos. Environ.,* 152, 77–84 (2017)

Haro, M., Cabal, B., Parra, J.B. and Ania, C.O. On the adsorption kinetics and equilibrium of polyaromatic hydrocarbons from aqueous solution. *Adsorpt. Sci. Technol.,* 29(5), 467–478 (2011)

Hayakawa, K. Environmental behaviors and toxicities of polycyclic aromatic hydrocarbons and nitropolycyclic aromatic hydrocarbons. *Chem. Pharm. Bull.,* 64, 83–94 (2016)

He, H., Wang, Y., Ma, Q.X., Ma, J.Z., Chu, B.W., Ji, D.S., Tang, G.Q., Liu, C., Zhang, H.X. and Hao, J.M. Mineral dust and NOx promote the conversion of SO_2 to sulfate in heavy pollution days. *Sci. Rep.,* 4, 4172 (2015)

He, J., Wang, H., Zhang, C., Yang, X.R., Shangguan, Y.F., Zhao, R., Gong, Y. and Wu, Z.X. A comprehensive analysis of the sedimentology, petrography, diagenesis and reservoir quality of sandstones from the Oligocene Xiaganchaigou (E3) Formation in the Lengdong area, Qaidam Basin, China. J. *Petrol. Explor. Prod. Technol.,* 9, 953–969 (2019)

Hellou, J. and Leonard, J. Polycyclic aromatic hydrocarbons bioaccumulation and biotransformation products in trout exposed through food pellets. *Polycycl. Aromat. Comp.,* 24, 697–712 (2004)

Huang, Y.D., Zhang, D.N., Duan, D.D., Yang, Y., Xiong, Y.Q. and Ran, Y. Importance of the structure and nanoporosity of organic matter on the desorption kinetics of

benzo[a]pyrene in sediments. *Environ. Pollut.,* 225, 628–636 (2017)

IARC (International Agency for Research on Cancer). IARC Monographs of the Evaluation of Carcinogenic Risks to Humans. Diesel and Gasoline Engine Exhausts. 2013IARC, vol. 105, World Health Organization, International Agency for Research on Cancer, Lyon, France. https://monographs.iarc.fr/wp-content/uploads/2018/06/mono105.pdf (2013)

Institute of Geographic Sciences and Natural Resources Research, Chinese Academy of Sciences (IGSNRR, CAS). Deserts in China. http://www.igsnrr.cas.cn/kxcb/dlyzykpyd/zgdl/zgdm/200704/t20070406_2154824.html (2007)

Islam, M.A. Diagenesis and reservoir quality of Bhuban sandstones (Neogene), Titas Gas Field, Bengal Basin, Bangladesh. *J. Asian Earth Sci.,* 35(1), 89–100 (2009)

Japan Meteorological Agency (JMA). Long-term trends of aeolian dust, updated on 12 February 2020. https://www.data.jma.go.jp/gmd/env/kosahp/en/kosa_shindan_e.html (2020)

Jariyasopit, N., Zimmermann, K., Schrlau, J., Arey, J., Atkinson, R., Yu, T.-W., Dashwood, R.H., Tao, S. and Massey Simonich, S.L. Heterogeneous reactions of particulate matter-bound PAHs and NPAHs with NO_3/N_2O_5, OH radicals, and O_3 under simulated long-range atmospheric transport conditions: reactivity and mutagenicity. *Environ. Sci. Technol.,* 48(17), 10155–10164 (2014)

Jeng, H.A., Pan, C.-H., Diawara, N., Chang-Chien, G.-P., Lin, W.-Y., Huang, C.-T., Ho, C.-K. and Wu, M.-T. Polycyclic aromatic hydrocarbon-induced oxidative stress and lipid peroxidation in relation to immunological alteration. *Occup. Environ. Med.,* 68, 653–658 (2011)

Jeong, G.Y. Bulk and single-particle mineralogy of Asian dust and a comparison with its source soils. *J. Geophys. Res.,* 113, D02208 (2008)

Jeong, G.Y. and Nousiainen, T. TEM analysis of the internal structures and mineralogy of Asian dust particles and the implications for optical modeling. *Atmos. Chem. Phys.,* 14, 7233–7254 (2014)

Jeong, G. Y. Mineralogy and geochemistry of Asian dust: Dependence on migration path, fractionation, and reactions with polluted air. *Atmos. Chem. Phys. Discuss.,* https://doi.org/10.5194/acp-2019-948 (2020)

Jia, H.Z., Li, L., Chen, H.X., Zhao, Y., Li, X.Y. and Wang, C.Y. Exchangeable cations-mediated photodegradation of polycyclic aromatic hydrocarbons (PAHs) on smectite surface under visible light. *J. Hazard. Mater.,* 287, 16–23 (2015)

Kalisa, E., Nagato, E.G., Bizuru, E., Lee, K.C., Tang, N., Pointing, S.B., Hayakawa, K., Archer, S.D.J. and Lacap-Bugler, D.C. Characterization and risk assessment of atmospheric $PM_{2.5}$ and PM_{10} particulate-bound PAHs and NPAHs in Rwanda, Central-East Africa. *Environ. Sci. Technol.,* 52(21), 12179–12187 (2018)

Kameda, T., Azumi, E., Fukushima, A., Tang, N., Matsuki, A., Kamiya, Y., Toriba, A. and Hayakawa, K. Mineral dust aerosols promote the formation of toxic nitropolycyclic aromatic compounds. *Sci. Rep.,* 6, 24427 (2016)

Khalili, N.R., Scheff, P.A. and Holsen, T.M. PAH source fingerprints for coke ovens, diesel and, gasoline engines, highway tunnels, and wood combustion emissions. *Atmos. Environ.,* 29, 533–542 (1995)

Kim, J.Y., Lee, J.Y., Choi, S.-D., Kim, Y.P. and Ghim, Y.S. Gaseous and particulate polycyclic aromatic hydrocarbons at the Gosan background site in East Asia. *Atmos. Environ.,* 49, 311–319 (2012a)

Kim, W.Y., Doh, S.-J. and Yu, Y.J. Asian dust storm as conveyance media of anthropogenic pollutants. *Atmos. Environ.,* 49, 41–50 (2012b)

Kurosaki, Y. and Mikami, M. Recent frequent dust events and their relation to surface wind

in East Asia. *Geophys. Res. Lett.,* 30, 1–2 (2003)

Lang, C., Tao, S., Liu, W., Zhang, Y. and Simonich, S. Atmospheric transport and outflow of polycyclic aromatic hydrocarbons from China. *Environ. Sci. Technol.,* 42, 5196–5201 (2008)

Li, B., Ou, P., Wei, Y., Zhang, X. and Song, J. Polycyclic aromatic hydrocarbons adsorption onto graphene: A DFT and AIMD Study. *Materials,* 11, 726 (2018)

Liu, C.Q., Masuda, A., Okada, A., Yabuki, S., Zhang, J. and Fan, Z.L. A geochemical study of loess and desert sand in northern China: Implications for continental crust weathering and composition. *Chem. Geol.,* 196, 359–374 (1993)

Liu, D.Y., Cao, D.F., Chen, S.Y., Zhou, B., Xia, J., Qian, H.Z. Effects of sand dust weather on air quality of cities in north bank of Taihu Lake. *J. Nat. Disaster,* 22(4), 135–144, (2013)

Liu, H., Xu, C., Jiang, Z.-Y. and Gu, A.H. Association of polycyclic aromatic hydrocarbons and asthma among children 6–19 years: NHANES 2001–2008 and NHANES 2011–2012. *Respir. Med.,* 110, 20–27 (2016)

Logan, D.T. Perspective on ecotoxicology of PAHs to fish. *Hum. Ecol. Risk Assess,* 13, 302–316 (2007)

Luo, H., Jia, L., Wan, Q., An, T.C. and Wang, Y.J. Role of liquid water in the formation of O_3 and SOA particles from 1,2,3-trimethylbenzene. *Atmos. Environ.,* 217, 116955 (2019)

Ma, J.Z., Liu, Y.C. and He, H. Degradation kinetics of anthracene by ozone on mineral oxides. *Atmos. Environ.,* 44(35), 4446–4453 (2010)

Ma, Q., Liu, Y.C., Liu, C., Ma, J.Z. and He, H. A case study of Asian dust storm particles: Chemical composition, reactivity to SO_2 and hygroscopic properties. *J. Environ. Sci.,* 24(1), 62–71 (2012)

Marquès, M., Mari, M., Audí-Miró, C., Sierra, J., Soler, A., Nadal, M. and Domingo, J.L.

Photodegradation of polycyclic aromatic hydrocarbons in soils under a climate change base scenario. *Chemosphere,* 148, 495–503 (2016)

Marquès, M., Mari, M., Sierra, J., Nadal, M. and Domingo, J.L. Solar radiation as a swift pathway for PAH photodegradation: a field study. *Sci. Total Environ.,* 581–582, 530–540 (2017)

Mastral, A.M. and Callén, M.S. A review on polycyclic aromatic hydrocarbon (PAH) emissions from energy generation. *Environ. Sci. Technol.,* 34(15), 3051–3057 (2000)

McCusker, L.B., Liebau, F. and Engelhardt, G. Nomenclature of structural and compositional characteristics of ordered microporous and mesoporous materials with inorganic hosts. *Pure Appl. Chem.,* 73(2), 381–394 (2001)

Meleshyn, A. and Tunega, D. Adsorption of phenanthrene on Na-montmorillonite: A model study. *Geoderma,* 169, 41–46 (2011)

Mmereki, B.T., Donaldson, D.J., Gilman, J.B., Eliason, T.L. and Vaida, V. Kinetics and products of the reaction of gas-phase ozone with anthracene adsorbed at the air–aqueous interface. *Atmos. Environ.,* 38(36), 6091–6103 (2004)

National Center for Biotechnology Information (NCBI). PubChem Database. Naphthalene, https://pubchem.ncbi.nlm.nih.gov/compound/naphthalene#section=Solubility (accessed on June 17, 2020)

Ngueleu, S.K., Rezanezhad, F., Al-Raoush, R.I. and Van Cappellen, P. Sorption of benzene and naphthalene on (semi)-arid coastal soil as a function of salinity and temperature. *J. Contam. Hydrol.,* 219, 61–71 (2018)

Nisbet, I.C.T. and Lagoy, P.K. Toxic equivalency factors (TEFs) for polycyclic aromatic hydrocarbons (PAHs). *Regul. Toxicol. Pharmacol.,* 16, 290–300 (1992)

Nishikawa, M., Kuga, N., Quan, H., Koyanagi, H., Onishi, K., Ukachi, M., Nagano, K., Mori, I. and Sano, T. Characteristics of color and chemical composition of surface soils

collected in source regions of Asian dusts and identification of the source of kosa aerosols transported to Japan. *J. Jpn. Soc. Atmos. Environ.,* 53(5), 165–185 (2018)

Nishino, N., Arey, J. and Atkinson, R. Formation and reactions of 2-formylcinnamaldehyde in the OH radical-initiated reaction of Nap. *Environ. Sci. Technol.,* 43(5), 1349–1353 (2009)

Oliva, P., Viers, J. and Dupré, B. Chemical weathering in granitic environments. *Chem. Geol.,* 202(3–4), 225–256 (2003)

Osada, K. Water soluble fraction of Asian dust particles. *Atmos. Res.,* 124, 101–108 (2013)

Pavanello, S. and Lotti, M. Internal exposure to carcinogenic polycyclic aromatic hydrocarbons and DNA damage. *Arch Toxicol.,* 87(3), 551–553 (2013)

Qian, Y., Posch, T. and Schmidt, T.C. Sorption of polycyclic aromatic hydrocarbons (PAHs) on glass surfaces. *Chemosphere,* 82(6), 859–865 (2011)

Qu, X.H., Zhang, Q.Z. and Wang, W.X. Mechanism for OH-initiated photooxidation of Nap in the presence of O_2 and NOx: a DFT study. *Chem. Phys. Lett.,* 429(1–3), 77–85 (2006)

Quintana, F., Basso, A., Iglesias, A., Korn, T., Farez, M.F., Bettelli, E., Caccamo, M., Oukka, M. and Weiner, H.L. Control of Treg and TH17 cell differentiation by the aryl hydrocarbon receptor. *Nature,* 453, 65–71 (2008)

Raja, S. and Valsaraj, K.T. Heterogeneous oxidation by ozone of naphthalene adsorbed at the air-water interface of micron-size water droplets. *J. Air Waste Manage.,* 55(9), 1345–1355 (2005)

Ren, Y.Q., Wang, G.H., Li, J.J., Wu, C., Cao, C., Li, J., Wang, J.Y., Ge, S.S., Xie, Y.N., Li, X.R., Meng, F. and Li, H. Evolution of aerosol chemistry in Xi'an during the spring dust storm periods: implications for heterogeneous formation of secondary organic aerosols on the dust surface. *Chemosphere,* 215, 413–421 (2019)

Reyes, C.A., Medina, M., Crespo-Hernandez, C., Cedeno, M.Z., Arce, R., Rosario, O.,

Steffenson, D.M., Ivanov, I.N., Sigman, M.E. and Dabestani, R. Photochemistry of pyrene on unactivated and activated silica surfaces. *Environ. Sci. Technol.,* 34(3), 415–421 (2000)

Ringuet, J., Albinet, A., Leoz-Garziandia, E., Budzinski, H. and Villenave, E. Reactivity of polycyclic aromatic compounds (PAHs, NPAHs and OPAHs) adsorbed on natural aerosol particles exposed to atmospheric oxidants. *Atmos. Environ.,* 61, 15–22 (2012)

Robles, H. Naphthalene, in: Wexler, P. (Eds.), Encyclopedia of Toxicology (Third Edition). Academic Press, pp. 437–439 (2014)

Romanias, M.N., Zeineddine, M.N., Gaudion, V., Lun, X.X., Thevenet, F. and Riffault, V. Heterogeneous interaction of isopropanol with natural Gobi dust. *Environ. Sci. Technol.,* 50(21), 11714–11722 (2016)

Saeedi, M., Li, L.Y. and Grace, J.R. Effect of organic matter and selected heavy metals on sorption of acenaphthene, fluorene and fluoranthene onto various clays and clay minerals. *Environ. Earth Sci.,* 77, 305 (2018)

Sasaki, J., Aschmann, S.M., Kwok, E.S.C., Atkinson, R. and Arey, J. Products of the gas-phase OH and NO_3 radical-initiated reactions of Nap. *Environ. Sci. Technol.,* 31(11), 3173–3179 (1997)

Shao, Y. and Dong, C.H. A review on East Asian dust storm climate, modelling and monitoring. *Global Planet. Change,* 52(1–4), 1–22 (2006)

Shen, Z.X., Cao, J.J., Arimoto, R., Zhang, R.J., Jie, D.M., Liu, S.X. and Zhu, C.S. Chemical composition and source characterization of spring aerosol over Horqin sand land in northeastern China. *J. Geophys. Res.,* 112, D14315 (2007)

Shi, H.X., Zhang, T.Y., Wang, H.L., Wang, X. and He, M. Photocatalytic conversion of naphthalene to α-naphthol using nanometer-sized TiO_2. *Chinese J. Catal.,* 32(1–2), 46–50 (2011)

Shiraiwa, M., Garland, R.M. and Pöschl, U. Kinetic double-layer model of aerosol surface chemistry and gas-particle interactions (K2-SURF): Degradation of polycyclic aromatic hydrocarbons exposed to O_3, NO_2, H_2O, OH and NO_3. *Atmos. Chem. Phys.,* 9, 9571–9586 (2009)

Shimada, K., Nohchi, M., Yang X.Y., Sugiyama, T., Miura, K., Takami, A., Sato, K., Chen, X., Kato, S., Kajii, Y., Meng, F. and Hatakeyama, S. Degradation of PAHs during long range transport based on simultaneous measurements at Tuoji Island, China, and at Fukue Island and Cape Hedo, Japan. *Environ Pollut.,* 260, 113906 (2020).

Smol, M. and Włodarczyk-Makuła, M. The effectiveness in the removal of PAHs from aqueous solutions in physical and chemical processes: a review. *Polycycl. Aromat. Comp.,* 37(4), 292–313 (2017)

Sofowote, U.M., Hung, H., Rastogi, A.K., Westgate, J.N., Deluca, P.F., Su, Y. and McCarry, B.E. Assessing the long-range transport of PAH to a sub-Arctic site using positive matrix factorization and potential source contribution function. *Atmos. Environ.,* 45(4), 967–976 (2011)

Sun, J.M. Provenance of loess material and formation of loess deposits on the Chinese Loess Plateau. *Earth Planetary Sci. Lett.,* 203(3–4), 845–859 (2002)

Sun, Y., Zhuang, G., Wang, Y., Zhao, X., Li, J., Wang, Z. and An, Z. Chemical composition of dust storms in Beijing and implications for the mixing of mineral aerosol with pollution aerosol on the pathway. *J. Geophys. Res.,* 110, D24209 (2005)

Tamamura, S., Sato, T., Ota, Y., Wang, X.L., Tang, N., and Hayakawa, K. Long-range transport of polycyclic aromatic hydrocarbons (PAHs) from the eastern Asian continent to Kanazawa, Japan with Asian dust. *Atmos. Environ.,* 41(12), 2580–2593 (2007)

Tang, D.L., Li, T.-Y., Liu, J.J. Chen, Y.-H., Qu, L.R. and Perera, F. PAH-DNA adducts in cord blood and fetal and child development in a Chinese cohort. *Environ. Health*

Perspec., 114, 8 (2006)

Tang, M.J., Cziczo, D.J. and Grassian, V.H. Interactions of water with mineral dust aerosol: water adsorption, hygroscopicity, cloud condensation, and ice nucleation. *Chem. Rev.,* 116(7), 4205–4259 (2016)

Tang, M.J., Zhang, H., Gu, W., Gao, J., Jian, X., Shi, G., Zhu, B.Q., Xie, L.H., Guo, L.Y., Zhe, W., Zhang, G.H. and Wang, X.M. Hygroscopic properties of saline mineral dust from different regions in China: geographical variations, compositional dependence, and atmospheric implications. *J. Geophys. Res. Atmos.,* 124, 10844–10857 (2019)

Tang, N., Hattori, T., Taga, R., Igarashi, K., Yang, X.Y., Tamura, K., Kakimoto, H., Mishukov, V.F., Toriba, A., Kizu, R. and Hayakawa, K. Polycyclic aromatic hydrocarbons and nitropolycyclic aromatic hydrocarbons in urban air particulates and their relationship to emission sources in the Pan-Japan Sea countries. *Atmos. Environ.,* 39, 5817–5826 (2005)

Tang, N., Sato, K., Tokuda, T., Tatematsu, M., Hama, H., Suematsu, C., Kameda, T., Toriba, A. and Hayakawa, K. Factors affecting atmospheric 1-, 2-nitropyrenes and 2-nitrofluoranthene in winter at Noto peninsula, a remote background site, Japan. *Chemosphere,* 107, 324–330 (2014)

Tang, N., Hakamata, M., Sato, K., Okada, Y., Yang, X., Tatematsu, M., Toriba, A., Kameda, T. and Hayakawa, K. Atmospheric behaviors of polycyclic aromatic hydrocarbons at a Japanese remote background site, Noto peninsula, from 2004 to 2014. *Atmos. Environ.,* 120, 144–151 (2015)

Tang, N., Suzuki, G., Morisaki, H., Tokuda, T., Yang, X.Y., Zhao, L.X., Lin, J., Kameda, T., Toriba, A. and Hayakawa, K. Atmospheric behaviors of particulate-bound polycyclic aromatic hydrocarbons and nitropolycyclic aromatic hydrocarbons in Beijing, China from 2004 to 2010. *Atmos. Environ.,* 152, 354–361 (2017)

Tuhkanen, T.A. and Beltrán, F.J. Intermediates of the oxidation of naphthalene in water with

the combination of hydrogen peroxide and UV radiation. *Chemosphere,* 30(8), 1463–1475 (1995)

Vialaton, D., Richard, C., Baglio, D. and Paya-Perez, A.-B. Mechanism of the photochemical transformation of Nap in water. *J. Photochem. Photobiol. A,* 123 (1–3), 15–19 (1999)

Vidal, C.B., Barros, A.L., Moura, C.P., de Lima, A.C.A., Dias, F.S., Vasconcellos, L.C.G., Fechine, P.B.A. and Nascimento, R.F. Adsorption of polycyclic aromatic hydrocarbons from aqueous solutions by modified periodic mesoporous organosilica. *J. Colloid Interf. Sci.,* 357(2), 466–473 (2011)

Wang, Z.F., Akimoto, H., Uno, I. Neutralization of soil aerosol and its impact on the distribution of acid rain over East Asia: observations and model results. *J. Geophys. Res.,* 107, (2002)

Wang, X.M., Hua, T., Zhang, C.X., Lang, L.L., and Wang, H.T. Aeolian salts in Gobi deserts of the western region of Inner Mongolia: gone with the dust aerosols. *Atmos. Res.,* 118, 1–9 (2012)

Wang, Q., Dong, X., Fu, J.S., Xu, J., Deng, C., Jiang, Y., Fu, Q., Lin, Y., Huang, K. and Zhuang, G. Environmentally dependent dust chemistry of a super Asian dust storm in March 2010: observation and simulation. *Atmos. Chem. Phys.,* 18, 3505–3521 (2018)

Wang, Y.D., Zhou, L., Wang, W.G. and Ge, M.F. Heterogeneous uptake of formic acid and acetic acid on mineral dust and coal fly ash. *ACS Earth Space Chem.,* 4(2), 202–210 (2020)

Wei, X.-Y., Liu, M., Yang, J., Du, W.-N., Sun, X., Huang, Y.-P., Zhang, X., Khalil, S.K., Luo, D.-M. and Zhou, Y.-D. Characterization of $PM_{2.5}$-bound PAHs and carbonaceous aerosols during three-month severe haze episode in Shanghai, China: Chemical composition, source apportionment and long-range transportation. *Atmos. Environ.,* 203, 1–9 (2019)

Williamson, C.J., Kupc, A., Axisa, D., Bilsback, K.R., Bui, T.P., Campuzano-Jost, P., Dollner, M., Froyd, K.D., Hodshire, A.L., Jimenez, J.L., Kodros, J.K., Lou, G., Murphy, D.M., Nault, B.A., Ray, E.A., Weinzierl, B., Wilson, J.C., Yu, F.Y., Yu, P.F., Pierce, J.R. and Brock, C.A. A large source of cloud condensation nuclei from new particle formation in the tropics. *Nature,* 574, 399–403 (2019)

Wilson, A.S., Davis, C.D., Williams, D.P., Buckpitt, A.R., Pirmohamed, M. and Park, B.K. Characterisation of the toxic metabolite(s) of naphthalene. *Toxicology,* 114, 233–242 (1996)

Wu, F., Zhang, D.Z., Cao, J.J., Xu, H.M. and An, Z.S. Soil-derived sulfate in atmospheric dust particles at Taklimakan desert. *Geophys. Res. Lett.,* 39, L24803 (2012)

Wu, S.-P., Schwab, J., Yang, B.-Y., and Yuan, C.-S. Effect of phenolic compounds on photodegradation of anthracene and benzo[a]anthracene in media of different polarity. *J. Photochem. Photobiol. A,* 309, 55–64 (2015)

Xu, L.-H., Wang, J.-H., Li, Y., Ma, Q.-L., Zhang, D.-K., Liu, Y.-J. and Fang, C. Variations of soil physical properties in desertification reversion process at south edge of Tengger Desert. *J. Desert Res.,* 28(4), 690–695 (2008)

Xu, X.M., Li, Y., Li, Y.Z., Lu, A.H., Qiao, R.X., Liu, K.H., Ding, H.R. and Wang, C.Q. Characteristics of desert varnish from nanometer to micrometer scale: A photo-oxidation model on its formation. *Chem. Geol.,* 522, 55–70 (2019)

Yakout, S.M., Daifullah, A.A.M. and El-Reefy, S.A. Adsorption of Nap, phenanthrene and pyrene from aqueous solution using low-cost activated carbon derived from agricultural wastes. *Adsorpt. Sci. Technol.,* 31(4), 293–302 (2013)

Yamashita, K., Murakami, M., Hashimoto, A. and Tajiri, T. CCN ability of Asian mineral dust particles and their effects on cloud droplet formation. *J. Meteorol. Soc. Jpn.,* 89, 581–587 (2011)

Yang, F.M., He, K.B., Lei, Y., Ma, Y.L., Yu, X.C., Shigeru, T., Tomoaki, O., Tamami, I. Chemical characters of atmospheric precipitation in Beijing in years of 2001~2003. *China Environ. Sci.,* 24(5), 538–541 (2004)

Yang, X.-Y., Okada, Y., Tang, N., Matsunaga, S., Tamura, K., Lin, J.-M., Kameda, T., Toriba, A. and Hayakawa, K. Long-range transport of polycyclic aromatic hydrocarbons from China to Japan. *Atmos. Environ.,* 41, 2710–2718 (2007)

Yang, X.-Y., Yamada, M., Tang, N., Lin, J.-M., Wang, W., T., Kameda, T., Toriba, A. and Hayakawa, K. Long-range transport of fluoride in East Asia monitored at Noto Peninsula, Japan. *Sci. Total Environ.,* 407(16), 4681–4686 (2009)

Yang, W.W., Ma, Q.X., Liu, Y.C., Ma, J.Z., Chu, B.W., Wang, L. and He, H. Role of NH_3 in the heterogeneous formation of secondary inorganic aerosols on mineral oxides. *J. Phys. Chem. A,* 122(30), 6311–6320 (2018)

Yin, S.S., Tang, M.L., Chen, F.F., Li, T.L. and Liu, W.P. Environmental exposure to polycyclic aromatic hydrocarbons (PAHs): The correlation with and impact on reproductive hormones in umbilical cord serum. *Environ. Pollut.,* 220, Part B, 1429–1437 (2017)

Zeineddine, M.N., Romanias, M.N., Riffault, V. and Thévenet, F. Heterogeneous interaction of various natural dust samples with isopropyl alcohol as a probe VOC. *J. Phys. Chem. A,* 122(22), 4911–4919 (2018)

Zhang, Y., Yang, B., Gan, J., Liu, C.G., Shu, X. and Shu, J.N. Nitration of particle-associated PAHs and their derivatives (nitro-, oxy-, and hydroxy-PAHs) with NO_3 radicals. *Atmos. Environ.,* 45(15), 2515–2521 (2011)

Zhang, D.N., Duan, D.D., Huang, Y.D., Yang, Y. and Ran, Y. Novel phenanthrene sorption mechanism by two pollens and their fractions. *Environ. Sci. Technol.,* 50(14), 7305–7314 (2016)

Zhang, L.L., Tokuda, T., Yang, L., Zhou, Q.Y., Zhang, X., Xing, W.L., Wu, Q., Zhou, Z.J., Chen, R.J., Kameda, T., Akira, T., Hayakawa, K. and Tang, N. Characteristics and health risks of particulate polycyclic aromatic hydrocarbons and nitro-polycyclic aromatic hydrocarbons at urban and suburban elementary schools in Shanghai, China. *Asian J. Atmos. Environ.,* 13, 266–275 (2019)

Zhang, L.L., Morisaki, H., Wei, Y.J., Li, Z.G., Yang, L., Zhou, Q.Y., Zhang, X., Xing, W.L., Hu, M., Shima, M., Akira, T., Hayakawa, K. and Tang, N. $PM_{2.5}$-bound polycyclic aromatic hydrocarbons and nitro-polycyclic aromatic hydrocarbons inside and outside a primary school classroom in Beijing: concentration, composition, and inhalation cancer risk. *Sci. Total Environ.,* 705, 135840 (2020a)

Zhang, X., Zhang, L.L., Yang, L., Zhou, Q.Y., Xing, W.L., Toriba, A., Hayakawa, K., Wei, Y.J. and Tang, N. Characteristics of polycyclic aromatic hydrocarbons (PAHs) and common air pollutants at Wajima, a remote background site in Japan. *Int. J. Environ. Res. Publ. Health,* 17, 957 (2020b)

Zhang, L.L., Zhang, X., Xing, W.L., Zhou, Q.Y., Yang, L., Nakatsubo, R., Wei, Y.J., Bi, J.R., Shima, M., Akira, T., Hayakawa, K. and Tang, N. Natural aeolian dust particles have no substantial effect on atmospheric polycyclic aromatic hydrocarbons (PAHs): A laboratory study based on naphthalene. *Environ. Pollut.,* 263, Part A, 114454 (2020c)

Zhao, S., Miao, D., Zhu, K.C., Tao, K.L., Wang, C.Y., Sharma, V.K. and Jia, H.Z., Interaction of benzo[a]pyrene with Cu(II)-montmorillonite: generation and toxicity of environmentally persistent free radicals and reactive oxygen species. *Environ. Int.,* 129, 154–163 (2019)

Zhou, S.M. and Wenger, J.C. Kinetics and products of the gas-phase reactions of acenaphthylene with hydroxyl radicals, nitrate radicals and ozone. *Atmos. Environ.,* 75, 103–112 (2013)

Zhou, L., Wang, W.G., Hou, S.Q., Tong, S.R. and Ge, M.F. Heterogeneous uptake of nitrogen dioxide on Chinese mineral dust. *J. Environ. Sci.,* 38, 110–118 (2015)

Zhu, D.D. and Zhou, Q.X. Action and mechanism of semiconductor photocatalysis on degradation of organic pollutants in water treatment: A review. *Environ. Nanotechnol. Monit. Manag.,* 12, 100255 (2019)

Acknowledgements

July 2020

Lulu Zhang

Dissertation Index

Reference theses

1) <u>**Zhang L.L.**</u>, Zhang X., Xing W.L., Zhou Q.Y., Yang L., Nakatsubo R., Wei Y.J., Bi J.R., Shima M., Toriba A., Hayakawa K., Tang N., Natural aeolian dust particles have no substantial effect on atmospheric polycyclic aromatic hydrocarbons (PAHs): A laboratory study based on naphthalene, *Environmental Pollution,* 263, 114454, August 2020.

Sub-theses

1) <u>**Zhang L.L.**</u>, Morisaki H., Wei Y.J., Li Z.G., Yang L., Zhou Q.Y., Zhang X., Xing W.L., Hu M., Shima M., Toriba A., Hayakawa K., Tang N., $PM_{2.5}$-bound polycyclic aromatic hydrocarbons and nitro-polycyclic aromatic hydrocarbons inside and outside a primary school classroom in Beijing: Concentration, composition, and inhalation cancer risk, *Science of the Total Environment,* 705, 135840, February 2020.

2) <u>**Zhang L.L.**</u>, Yang L., Zhou Q.Y., Zhang X., Xing W.L., Wei Y.J., Hu M., Zhao L.X., Toriba A., Hayakawa K., Tang N., Size distribution of particulate polycyclic aromatic hydrocarbons in fresh combustion smoke and ambient air: A review, *Journal of Environmental Sciences,* 88, 370-384, February 2020.

3) <u>**Zhang L.L.**</u>, Tokuda T., Yang L., Zhou Q.Y., Zhang X., Xing W.L., Wu Q., Zhou Z.J., Chen R.J., Kameda T., Toriba A., Hayakawa K., Tang N., Characteristics and Health Risks of Particulate Polycyclic Aromatic Hydrocarbons and Nitro-polycyclic Aromatic Hydrocarbons at Urban and Suburban Elementary Schools in Shanghai, China, *Asian Journal of Atmospheric Environment,* 13, 266-275, December 2019.

4) <u>**Zhang L.L.**</u>, Morisaki H., Wei Y.J., Li Z.G., Yang L., Zhou Q.Y., Zhang X., Xing W.L., Hu M., Shima M., Toriba A., Hayakawa K., Tang N., Characteristics of air pollutants inside and outside a primary school classroom in Beijing and respiratory health impact on children, *Environmental Pollution,* 255, 113147, December 2019.